International Journal of Biological Macromolecules 339 (2026) 149851

Contents lists available at ScienceDirect

International Journal of Biological Macromolecules

journal homepage: www.elsevier.com/locate/ijbiomac

Zinc cofactor in human histone deacetylase 8: Requirement for function and opportunity for drug discovery

Paula M. Garcia-Franco [a,b], F. Javier Falcó-Martí [a], Hajar Jeblaoui [a,c], Marta Asencio del Rio [a,c], David Ortega-Alarcon [a,c], Sonia Vega [a], Juan J. Galano-Frutos [a,b], Olga Abian [a,c,d,e,*], Adrian Velazquez-Campoy [a,c,d,e,*]

[a] Institute of Biocomputation and Physics of Complex Systems (BIFI), Universidad de Zaragoza, 50018, Zaragoza, Spain
[b] Certest Biotec S.L., 50840, San Mateo de Gallego, Zaragoza, Spain
[c] Institute for Health Research Aragon (IIS Aragon), 50009, Zaragoza, Spain
[d] Networking Biomedical Research Centre in Liver and Digestive Diseases (CIBERehd), 28029, Madrid, Spain
[e] Department of Biochemistry and Molecular and Cell Biology, University of Zaragoza, 50009, Zaragoza, Spain

ARTICLE INFO

Keywords:
Histone deacetylase 8
Zinc-dependent protein
Conformational equilibrium
Binding equilibrium
Calorimetry
Molecular dynamics simulations

ABSTRACT

HDAC8 (histone deacetylase 8), a class I HDAC, is a promising target for different disorders: X-linked intellectual disability, fibrotic disease, cancer, and several neuropathological diseases. The structural and functional similarity between HDACs hinders the development of selective HDAC8 inhibitors. To date, no drugs based on competitive inhibition have been approved. In order to identify weaknesses in HDAC8 amenable to drug discovery, we report here a comprehensive thermodynamic characterization of the structural stability and its modulation by the interaction with its zinc (Zn^{2+}) cofactor using a combination of experimental and computational techniques. HDAC8 represents an interesting example of an allosteric protein in the broad sense, in which its cofactor, the zinc ion, modulates its conformational equilibrium. The native, inactive, zinc-free state is physiologically relevant considering that the intracellular concentration of zinc is very low and may constitute a valid target for drug discovery.

1. Introduction

Post-translational modifications (PTMs) of histones, including covalent modification, such as methylation, phosphorylation, acetylation, ubiquitination, and SUMOylation, are key epigenetic marks. In particular, histone acetylation and deacetylation, the most common and well-studied events related to histone modifications, alter chromatin structure and regulate gene expression [1,2]. Lysine residues located on the N-terminal tail protruding from the nucleosome histone core are acetylated and deacetylated as part of gene regulation by histone acetyltransferases (HATs) and histone deacetylases (HDACs). Deacetylation restores a positive charge to specifically acetylated lysines, promoting the interaction of the histone N-terminal ends with negatively charged phosphate groups of DNA and negatively charged regions in histones. This results in the conversion of decondensed, loosely packed, transcriptionally active chromatin (euchromatin) to condensed, tightly packed, transcriptionally inactive chromatin (heterochromatin) [3–5]. Besides histones, HDACs also deacetylate non-histone protein substrates [6,7].

Because of their fundamental role in regulating chromatin structure and gene expression, HDACs are important in many biological processes, such as stress response, apoptosis, senescence, proliferation, differentiation, and DNA repair, among many others. HDAC dysfunction and impaired acetylation and deacetylation lead to the development of numerous disorders, including cancer, inflammatory and neurological disorders, as well as heart and pulmonary diseases [8,9]. Therefore, HDACs have been considered drug targets for many diseases.

There are at least 18 human HDACs that are classified according to their similarity in amino acid sequence to yeast factors, number of active catalytic sites, and cofactor dependence [10,11]: class I (HDAC 1–3 and HDAC8), class IIa (HDAC4, HDAC5, HDAC7 and HDAC9), class IIb (HDAC6 and HDAC10), class III (SIRT1–7), and class IV (HDAC11). HDACs from classes I, II, and IV are metalloenzymes that require a divalent metal ion (e.g., Zn^{2+} or Mn^{2+}) for substrate binding and

* Corresponding authors at: Institute of Biocomputation and Physics of Complex Systems (BIFI), Universidad de Zaragoza, 50018, Zaragoza, Spain.
E-mail addresses: oabifra@unizar.es (O. Abian), adrianvc@unizar.es (A. Velazquez-Campoy).

https://doi.org/10.1016/j.ijbiomac.2025.149851
Received 11 September 2025; Received in revised form 4 December 2025; Accepted 20 December 2025
Available online 22 December 2025

catalysis. The class III enzymes, termed sirtuins due to their homology with yeast Sir2 [7], have a protein fold and a catalytic mechanism differing from those of class I, II, and IV enzymes. Class I HDACs are ubiquitously expressed and are primarily located in the nucleus, while class II HDACs can shuttle between nucleus and cytoplasm and demonstrate tissue-specific expression.

HDAC8 is the latest member of class I HDAC to be identified and studied [12–14]. HDAC8 performs critical roles in human gene transcription and pathophysiology involved in various cellular homeostatic mechanisms. The Structural Maintenance of Chromosome 3 (SMC3), a subunit of the cohesion complex, is one of the best characterized targets of HDAC8 [15–17]. Estrogen-Related Receptor alpha (ERRα) and p53 have been reported to be either substrates or interaction partners of HDAC8 [15,18]. HDAC8 is overexpressed or deregulated in various types of cancers, such as melanoma, hepatocellular carcinoma, gastric cancer, oral squamous cell carcinoma, breast cancer, lung cancer, malignant T-cell neoplasms, and childhood neuroblastoma, and is also associated with events related to drug resistance [19–24]. Therefore, HDAC8 inhibitors should be valuable weapons in the fight against these diseases.

The structure of HDAC8 consists of a single compact α/β domain composed of a central eight-stranded parallel beta-sheet and eleven α-helices [25]. A zinc-binding site harboring the required cofactor for catalytic activity and two potassium binding sites enhancing the structural stability are interconnected and determine its enzymatic activity [25]. The active site of HDAC8 comprises a hydrophobic tunnel containing the catalytic machinery [16].

Several inhibitors of metal-dependent HDACs have been approved for cancer chemotherapy, all of them targeting the active site zinc ion [26–29]. Vorinostat, Belinostat, and Panobinostat contain hydroxamic acid moieties that chelate zinc, and Romidepsin is a cyclic depsipeptide that, in its reduced form, contains a thiol group that coordinates zinc. These inhibitors are non-selective with respect to particular HDAC isozymes, in addition to chelating zinc unspecifically. Therefore, their use may cause unwanted side effects [30]. Consequently, the development of isozyme selectivity in HDAC inhibitors is a priority for current drug design efforts.

Zinc is an essential element required for many protein structures and catalytic functions involved in cell division and DNA and protein synthesis, among others. In eukaryotic organisms, up to 10 % of proteins are zinc-dependent proteins [31,32]. Zn^{2+} plays a dual role: it contributes to the overall structural stability of the protein and, in many cases, participates in the molecular mechanism underlying protein activity (e.g., many metalloproteases). Structural Zn^{2+} sites predominantly contain cysteine residues, while catalytic Zn^{2+} sites mainly contain histidine residues. In the case of HDAC8, Zn^{2+} is coordinated by two aspartic residues (D178 and D267) and one histidine residue (H180), in addition to a water molecule trapped in the active site [25].

Because small divalent cations, such as Zn^{2+}, are highly polarizing atoms (high charge density in a small atomic volume), zinc binding sites in proteins contain many polar or charged residues that coordinate the specific cation. Therefore, metal-dependent proteins may undergo considerable conformational changes upon metal association/dissociation [33], often involving partially or fully unfolded metal-unbound protein states. Zinc-dependent proteins are no exception, and zinc modulates their conformational landscape by inducing population shifts towards those conformational states that preferentially interact with the cation. Thus, zinc-dependent proteins can populate at least three main conformational states that comprise their conformational landscape: zinc-free native state, zinc-bound native state, and zinc-free unfolded state. Very often, the zinc-free native state corresponds to a partially unfolded and inactive conformation [34–37]. Because each protein conformational state is characterized by a specific function (or absence of function), the conformational landscape can be mapped onto a functional landscape, in which protein molecules are distributed among conformational and functional states exhibiting different activities.

The intracellular pool of free Zn^{2+} is under tight and strict control, resulting in a very low (well below the nanomolar level) concentration [38,39]. As a result, Zn^{2+}-dependent proteins are subjected to considerable chemical stress, and their Zn^{2+}-free conformational states (inactive native state and unfolded state) could be physiologically relevant from a quantitative and statistical point of view, besides the fact that they constitute inactive or dysfunctional states of zinc-dependent proteins.

There is a need to identify new HDAC8 inhibitors as potential drugs for transcriptional therapy and cancer chemoprevention. In order to develop isozyme selectivity in HDAC inhibitors, new structural/functional elements in HDACs, such as exosites or allosteric sites, or new conformational targets, can be considered as hot spots for drug discovery. To achieve this goal, we report a comprehensive biophysical study of HDAC8 and its interaction with zinc, which provides valuable information for considering the zinc-free HDAC8 conformation as a drug target.

2. Materials and methods

2.1. Expression and purification

The HDAC8 gene (1–377 residues) (NCBI Reference Sequence: NP_060956.1) was amplified to insert a PreScission Protease cleavage site (Leu-Glu-Val-Leu-Phe-Gln-Gly-Pro) and a hexahistidine tag at the C terminus. It was cloned into pET-30a(+) via *Nde*I and *Xho*I by GenScript. Plasmids were transformed into BL21 (DE3) *Escherichia coli* strain which were incubated in LB/Kan plates (50 μg/mL kanamycin) at 37 °C overnight. Cell culture was performed in liquid medium [40]: Terrific Broth (TB) rich medium (12 g/L tryptone, 24 g/L yeast extract, 0.4 % v/v glycerol), supplemented with 10 % v/v salt medium (phosphate buffer: 0.17 M potassium phosphate monobasic, 0.72 M potassium phosphate dibasic, pH 7.5) [40]. Kanamycin was added to reach a final concentration of 50 μg/mL. Induction was initiated when reaching an OD_{600} of approximately 0.6 absorbance units: after 1 h at 4 °C protein expression was induced by adding isopropyl-1-thio-β-D-galactopyranoside (IPTG) (Merck-Sigma) and $ZnCl_2$ (Merck-Sigma) at 400 μM and 100 μM concentration, respectively, and harvested after 22 h incubation at 18 °C. Cells were collected by centrifugation (10 min, 6000*g* at 4 °C). Harvested bacteria were resuspended in lysis buffer (25 mM Tris/HCl pH 7, 250 mM KCl) supplemented with protease inhibitors cocktail (PMFS 100 μM (Merck-Sigma), Benzamidine 1 mM (Merck-Sigma) and Leupeptin 5 μM (Peptide Institute INC)) and frozen at −20 °C until further use.

After thawing, 1 mg/mL lysozyme and 3 U/mL benzonase were added, and cell lysis was carried out by sonication (Vibra-Cell Ultrasonic Liquid Processor, Sonics) on ice and clarified by centrifugation at 19500 rpm for 45 min (Gyrozen, High-Speed Centrifuge 2236R). The supernatant was filtered through a 0.45 μm-pore filter to remove large impurities and aggregates and loaded into a HiTrap Talon column (GE-Healthcare Life Sciences) preequilibrated with binding buffer (25 mM Tris/HCl pH 7, 250 mM KCl, 15 mM imidazole). HDAC8 was eluted with a gradient of imidazole up to 300 mM. Serial dialysis for buffer exchange was performed to finally obtain HDAC8 in buffer 10 mM Tris/HCl pH 7, 20 mM KCl. All studies were carried out studying HDAC8 in the same conditions for the native Zn^{2+}-bound HDAC8 (HDAC8 with endogenous zinc from protein expression) and adding 100 μM ethylenediamine tetraacetic acid (EDTA) for obtaining Zn^{2+}-free HDAC8. In some cases, an additional dialysis to remove EDTA was required (e.g., for performing the ITC experiments). The identity of the protein was verified by mass spectrometry (MALDI-TOF/TOF) in the proteomics technical service at the Centro de Investigación Biomédica de Aragón (CIBA).

2.2. Analytical size exclusion chromatography (SEC)

Superdex 200 Increase 10/300GL (Cytiva) was used in order to determine HDAC8 molecular mass in 10 mM Tris pH 7, 20 mM KCl, in

the presence and absence of Zn^{2+}. Gel filtration standard cat#151-1901 (Bio-Rad) was employed as the molecular mass protein standard.

2.3. Circular dichroism spectroscopy (CD)

Spectra were collected by using a thermostated Chirascan spectropolarimeter (Applied Photophysics) equipped with a Peltier temperature control. The assays were carried out in the far-UV range (200–260 nm) and the near-UV range (250–310 nm) using a 0.1 cm and a 1 cm path-length quartz cuvette (Hellma), respectively, and a protein concentration of 10 μM. For thermal denaturation experiments, a temperature scan from 12 to 85 °C was performed at 222 nm with a scanning rate of 1 °C/min. The apparent unfolding parameters for HDAC8 in the absence and the presence of zinc were estimated applying the single transition model [41]:

$$\Delta G(T) = \Delta H(T_m)\left(1 - \frac{T}{T_m}\right) + \Delta C_P\left(T - T_m - T\ln\frac{T}{T_m}\right)$$
$$\langle X\rangle = \frac{X_N + X_U exp(-\Delta G(T)/RT)}{1 + exp(-\Delta G(T)/RT)} \quad (1)$$

where ΔG is the unfolding Gibbs energy, ΔH is the unfolding enthalpy, T_m is the unfolding temperature, ΔC_P is the unfolding heat capacity, $<X>$ is the measured signal at each temperature, X_N and X_U are the intrinsic signals for the native and the unfolded states, which are considered linear functions of the temperature.

2.4. Fluorescence spectroscopy

Assays were carried out using a Cary Eclipse Fluorescence Spectrophotometer (Varian) using a 1 cm path-length quartz cuvette (Hellma). Fluorescence emission spectra were recorded from 300 to 500 nm using an excitation wavelength of 290 nm and a bandwidth of 5 nm, with a protein concentration of 10 μM. Using the same instrument, fluorescence emission spectra using 1-anilino-8-naphthalene sulfonic acid (ANS) as extrinsic fluorescence probe were recorded from 400 to 700 nm using an excitation wavelength of 370 nm and a bandwidth of 5 nm, with a protein concentration of 10 μM and an ANS concentration of 100 μM. In both cases the samples were incubated for 30 min at room temperature before analysis. For chemical unfolding studies, assays were carried out using a SpectraMax iD5 plate reader (Molecular Devices). Protein at 10 μM concentration was incubated for 2 h at room temperature with increasing concentration of urea (from 0 to 5.5 M) and the fluorescence emission intensity at an emission wavelength of 340 nm was measured with an excitation wavelength of 280 nm. The apparent unfolding parameters for HDAC8 in the absence and the presence of Zn^{2+} were estimated applying the single transition model and the linear extrapolation model for chemical denaturation [41]:

$$\Delta G([D]) = \Delta G - m[D]$$
$$\langle X\rangle = \frac{X_N + X_U exp(-\Delta G([D])/RT)}{1 + exp(-\Delta G([D])/RT)} \quad (2)$$

where ΔG is the unfolding Gibbs energy, m is the susceptibility of the protein to the denaturant, $[D]$ is the denaturant concentration, $<X>$ is the measured signal at each temperature, X_N and X_U are the intrinsic signals for the native and the unfolded states, which are considered linear functions of the denaturant concentration.

2.5. Differential scanning fluorimetry (DSF)

Thermal unfolding experiments were conducted in a Mx3005P real-time qPCR thermocycler (Agilent Technologies) using SYPRO Orange (Thermo Fisher Scientific) as an extrinsic fluorescent amphipathic probe. Emission fluorescence was measured at 610 nm with excitation at 492 nm using a scanning rate of 1 °C/min with a protein concentration of 2 μM and a SYPRO Orange concentration of 5× (~10 μM, [42]). The apparent unfolding parameters for HDAC8 in the absence and the presence of Zn^{2+} were estimated applying the single unfolding transition model as explained above (Eq. (1)).

2.6. Differential scanning calorimetry (DSC)

The heat capacity of HDAC8 solutions, taking that of the buffer solution as a reference, was measured as a function of temperature using an Auto-PEAQ-DSC (MicroCal, Malvern-Panalytical). Assays were performed at a scanning rate of 1 °C/min with a protein concentration of 10 μM. The raw thermogram was normalized by protein concentration and baseline-corrected by subtracting a buffer scan. A model-free preliminary analysis based on the van 't Hoff unfolding enthalpy (ΔH_{vH}) was performed first:

$$\Delta H_{vH}(T) = \frac{4RT_m^2\Delta C_{P,max}}{\Delta H(T_m)} \quad (3)$$

where R is the ideal gas constant, T_m is the apparent unfolding temperature, $\Delta C_{P,max}$ is the maximal heat capacity, and $\Delta H(T_m)$ is the calorimetric unfolding enthalpy (area under the unfolding curve). Similar values for the van 't Hoff and calorimetric unfolding enthalpies indicate that the unfolding process consists of a single unfolding transition with no relevant intermediate partially (un)folded conformational states. A van 't Hoff enthalpy smaller than the calorimetric enthalpy indicates that the unfolding process consists of more than one unfolding transition with relevant intermediate partially (un)folded conformational states. A van 't Hoff enthalpy larger than the calorimetric enthalpy indicates that the unfolding process involves the dissociation of an oligomeric protein, or the dissociation of a ligand bound to the native state.

Thermal unfolding curves were analyzed considering a single transition equilibrium unfolding model for the Zn^{2+}-free protein, which is coupled to a single site equilibrium Zn^{2+}-binding model for the Zn^{2+}-bound protein. Briefly, the partition function for the unfolding equilibrium of a protein coupled to the ligand binding equilibrium is given by [43,44]:

$$Z(T) = 1 + \frac{K(T)}{1 + K_B(T)[L]} \quad (4)$$

where K is the intrinsic unfolding equilibrium constant, K_B is the ligand binding equilibrium constant, and $[L]$ is the concentration of free ligand (Zn^{2+} in this case). The average molar unfolding enthalpy of the system is given by the first derivative of the partition function with respect to the temperature:

$$\langle\Delta H\rangle(T) = RT^2\frac{\partial \ln Z(T)}{\partial T} = F_U(T)(\Delta H(T) - F_B(T)\Delta H_B(T)) \quad (5)$$

where F_U is the fraction of unfolded protein, F_B is the fraction of ligand-bound native protein, ΔH is the unfolding enthalpy for the ligand-free protein, and ΔH_B is the ligand binding enthalpy. The average molar unfolding heat capacity of the system, the magnitude measured by DSC, is given by the temperature derivative of the enthalpy:

$$\langle\Delta C_P\rangle(T) = \frac{\partial\langle\Delta H\rangle(T)}{\partial T} \quad (6)$$

The presence of the ligand modulates the unfolding thermodynamic parameters giving rise to apparent parameters for the unfolded state:

$$\Delta G^{app} = \Delta G + RT\ln(1 + K_B[L]) = \Delta G - \langle\Delta G_B\rangle$$
$$\Delta H^{app} = \Delta H - F_B\Delta H_B = \Delta H - \langle\Delta H_B\rangle$$
$$\Delta C_P{}^{app} = \Delta C_P - F_B\Delta C_{P,B} - F_B(1 - F_B)\frac{\Delta H_B^2}{RT^2} = \Delta C_P - \langle\Delta C_{P,B}\rangle \quad (7)$$

where $\Delta C_{P,B}$ is the binding heat capacity. The apparent unfolding

parameters correspond to the combination of the intrinsic unfolding parameters with the average contributions from ligand binding (terms with brackets).

In the real scenario, the total concentration of the ligand is limited and, therefore, the overall equilibrium must be solved:

$$\begin{aligned}[P]_T &= [N] + [U] + [NL] = [N](1 + K + K_B[L]\,) \\ [L]_T &= [L] + [NL] = [L](1 + K_B[N]\,)\end{aligned} \tag{8}$$

where $[P]_T$ is the total protein concentration, $[L]_T$ is the total ligand concentration, N is ligand-free native state, U is the unfolded state, and NL is the ligand-bound native state. Thus, employing the temperature dependence of the thermodynamic parameters:

$$\begin{aligned}\Delta H(T) &= \Delta H(T_m) + \Delta C_P(T - T_m) \\ K(T) &= e^{-\left(\Delta H(T_m)\left(1-\frac{T}{T_m}\right)+\Delta C_P\left(T-T_m-T\ln\frac{T}{T_m}\right)\right)\Big/RT} \\ \Delta H_B(T) &= \Delta H_B(T_0) + \Delta C_P(T - T_0) \\ K_B(T) &= K_B(T_0)\, e^{-\left(\Delta H_B(T_0)\left(1-\frac{T}{T_0}\right)+\Delta C_{P,B}\left(T-T_0-T\ln\frac{T}{T_0}\right)\right)\Big/RT}\end{aligned} \tag{9}$$

and solving the chemical equilibrium at each temperature, the fractions of the unfolded and ligand-bound states (F_U and F_B) can be calculated at each temperature (Eq. (8)):

$$\begin{aligned}F_N &= \frac{[N]}{[P]_T} \\ F_B &= \frac{[NL]}{[P]_T} \\ F_U &= \frac{[U]}{[P]_T}\end{aligned} \tag{10}$$

Then, the average unfolding enthalpy can be calculated using Eq. (5) and the average unfolding heat capacity can be calculated using Eq. (6), which can be easily evaluated numerically. The two temperatures T_m and T_0 are reference temperatures for conformational equilibrium and binding equilibrium, respectively; normally, T_m is taken as the unfolding temperature ($K(T_m) = 1$, $\Delta G(T_m) = 0$), and T_0 is taken as 25 °C due to practical purposes.

Non-linear least-squares regression data analysis provided estimations of the thermodynamic stability parameters (unfolding temperature, T_m; unfolding enthalpy $\Delta H(T_m)$; and unfolding heat capacity, ΔC_P), which allowed outlining the temperature stability profile (Gibbs energy of stabilization, ΔG, as a function of temperature), as well as the thermodynamic binding parameters for Zn^{2+} binding (binding constant, K_B; binding enthalpy, ΔH_B; and binding heat capacity, $\Delta C_{P,B}$) in the case of HDAC8 in the presence of zinc. By imposing $[L]_T = 0$ (or $K_B = 0$, $\Delta H_B = 0$, $\Delta C_{P,B} = 0$) in Eqs. (5)–(9), the simple single-transition unfolding model for the protein in the absence of ligand (i.e., Zn^{2+}-free HDAC8) is recovered.

2.7. Isothermal titration calorimetry (ITC)

The interaction between HDAC8 and Zn^{2+} was assessed in a high-sensitivity Auto-iTC200 (MicroCal, Malvern-Panalytical). Calorimetric titrations were carried out in buffer 10 mM Tris pH 7, 20 mM KCl. HDAC8 in the cell at 10 μM was titrated with 100 μM Zn^{2+} in the syringe. A sequence of 19 injections of 2 μL of titrant solution spaced evenly over 150 s was programmed with a stirring speed of 750 rpm and a reference power of 10 μcal/s.

Data analysis was performed applying the single ligand binding site model [45]. Briefly, the concentration of ligand and protein inside the calorimetric cell after each injection j are calculated as follows:

$$\begin{aligned}[L]_{Tj} &= [L]_{syr}\left(1 - \prod_{k=1}^{j}\left(1 - \frac{v_k}{V_0}\right)\right) \\ [P]_{Tj} &= [P]_{cell}\prod_{k=1}^{j}\left(1 - \frac{v_k}{V_0}\right)\end{aligned} \tag{11}$$

where $[L]_{syr}$ is the concentration of ligand in the syringe, $[P]_{cell}$ is the initial concentration of protein in the cell, v_k is the volume of each injection, V_0 is the cell volume, and j is the injection number. Normally, a factor n multiplying $[P]_{cell}$ is included in Eq. (11) to account for a fraction of non-binding-competent protein in the calorimetric cell. The binding isotherm (ligand-normalized injection heats as a function of the molar ratio) was built by integrating the injection heat effects recorded in the thermogram (thermal power as a function of time) and the theoretical heat effect was calculated as follows:

$$Q_j = \frac{1}{v_j[L]_{syr}}V_0\Delta H_B\left([PL]_j - [PL]_{j-1}\left(1 - \frac{v_j}{V_0}\right)\right) + Q_d \tag{12}$$

where $[PL]_j$ is the concentration of complex formed after injection j and Q_d is the background injection heat (usually called "dilution heat", but it includes many other unspecific phenomena such as mechanical mixing and buffer neutralization). The concentration of complex after each injection was calculated by solving the chemical equilibrium, using the concentrations calculated with Eq. (11):

$$\begin{aligned}[P]_T &= [P] + [PL] = [P](1 + K_B[L]\,) \\ [L]_T &= [L] + [PL] = [L](1 + K_B[P]\,)\end{aligned} \tag{13}$$

This set of equations leads to the well-known quadratic equation for the binding equilibrium with a single ligand binding site:

$$[L]_T = [L] + [P]_T\frac{K_a[L]}{1 + K_a[L]} \tag{14}$$

from which the concentration of free ligand $[L]$ can be calculated, as well as the concentration of complex:

$$[PL] = [P]_T\frac{K_a[L]}{1 + K_a[L]} \tag{15}$$

Non-linear least-squares regression data analysis provided estimations of the thermodynamic binding parameters for Zn^{2+} binding to HDAC8 (binding constant, K_B; binding enthalpy, ΔH_B; and apparent binding stoichiometry, n).

2.8. Activity assay

The catalytic activity of HDAC8 was assessed through fluorescence measurements using a SpectraMax iD5 (Molecular Devices) and the CycLex HDACs Deacetylase Fluorometric Assay Kit (MBL Life Science) in 96-well plates (Thermo Fisher Scientific). This kit consists in the coupling of the deacetylation reaction with a proteolytic reaction. Briefly, HDAC8 releases the acetate moiety from an ε-acetylated lysine residues in the peptide substrate, and the unprotected lysine-deacetylated peptide is cleaved by trypsin releasing 7-amino-4-methylcoumarin (AMC), which can be detected by measuring fluorescence intensity at an emission wavelength of 460 nm and an excitation wavelength of 390 nm. Assays were performed with a Zn^{2+}-bound and Zn^{2+}-free HDAC8 at a concentration of 0.2 μM and a substrate concentration of 20 μM in a final reaction volume of 50 μL per well. To avoid interference of EDTA/Zn^{2+} with the assay, Zn^{2+}-free HDAC8 was dialyzed to remove all remaining EDTA (free EDTA and EDTA/Zn^{2+} complex). Fluorescence intensity was recorded continuously for 60 min, with readings taken every minute at a constant temperature of 25 °C.

2.9. Molecular dynamics simulations (MDS)

System preparation. The three-dimensional structure of HDAC8 (UniProtKB entry: Q9BY41) available in the Protein Data Bank entry 1T64 [16] (resolution 1.90 Å) was used as the starting conformation for MDS. The asymmetric unit of this PDB structure consists of two HDAC8 chains (A and B), both lacking the first thirteen residues of the full-length protein sequence. Chain A was selected for MDS, and crystal water molecules, Ca^{2+} and Na^{+} ions, as well as trichostatin A molecules were removed from the structure. Missing side chains of incomplete amino acids were modelled using UCSF ChimeraX [46], and protonation states at pH 7 were assigned by the PropKa program [47,48] integrated in the APBS-PDB2PQR suite [49,50].

Two distinct HDAC8 systems were prepared: one Zn^{2+}-bound and one Zn^{2+}-free. In the Zn^{2+}-bound HDAC8 system, the Zn^{2+} ion was preserved in its experimentally determined coordination environment, as resolved in PDB 1T64, and the entire metal center was parameterized using the MCPB.py program [51] from the AmberTools24 package [52]. Geometry optimization, force constants derivation, and charge calculation for the metal center were performed at the quantum mechanical (QM) level using Gaussian 16 [53] (see additional details in the Supporting information). The Amber ff19SB force field [54] was employed to assign parameters for the rest of the protein in the Zn^{2+}-bound system and for the entire HDAC8 protein in the Zn^{2+}-free system. The simulations were performed with GROMACS 2024.3 package [55–57], installed on the *Agustina* cluster (BIFI Institute, University of Zaragoza), which is part of the "Red Española de Supercomputación" (RES).

Both systems were prepared in a dodecahedral box, ensuring a minimum distance of 2 nm between the protein and the box edge. Explicit TIP3P water molecules [58] were used for solvation. The net charges of the Zn^{2+}-bound and Zn^{2+}-free HDAC8 systems were − 4 and − 6, respectively. Na^{+} and Cl^{-} counterions were added to neutralize the systems and simultaneously achieve an ionic strength of 0.15 M, thereby mimicking physiological conditions. For the ions, parameters developed by Merz et al. were applied [59].

Energy minimization was performed using the steepest descent algorithm [55–57], until the convergence criterion was met. Three replicas were prepared for each system, which were gradually heated—starting from random initial velocities—using a ladder-like temperature ramp (increments of 50 K every 25 ps), until reaching the target temperature of 298 K. During this NVT step (time_step = 1 fs), temperature coupling was applied using the V-rescale thermostat (τ_T = 0.1 ps) [60]. Subsequently, two additional equilibration phases were carried out: 1) a 100 ps NPT phase using the Berendsen barostat [61] to weakly couple the system pressure to 1 atm, and 2) a 200 ps NPT phase at 1 atm using the more accurate Parrinello−Rahman barostat (τ_P = 5.0 ps) [62], both with a timestep of 2 fs. Periodic boundary conditions (PBC) were applied in all directions. Short-range electrostatics were treated using a cutoff radius of 1.2 nm, while long-range electrostatic were calculated using the Particle Mesh Ewald (PME) method [63]. Van der Waals interactions were handled using a cutoff radius of 1.2 nm, with a potential-shift modifier in combination with the Verlet cutoff-scheme. Constraints were applied to all bonds during the NVT heating step and to all bonds involving hydrogens during the subsequent NPT phases, including the production run. The LINCS algorithm (with lincs_order = 8) was used for this purpose [64]. Additional details of the MDS setup are described in the Supporting information.

Production phase and analyses. Five-microsecond NPT production runs (time_step = 2 fs), starting from the final configuration of the equilibration phase, were performed for both HDAC8 systems, and the resulting trajectories were used for subsequent analyses. Coordinates were recorded in .xtc trajectory files every 1 ns, while the system energy was saved every 50 ps.

The Python-based reMoDA workflow (https://github.com/elhectro2/reMoDA) [65], designed for multi-parametric analysis (the main working module) and the detection of unfolding events in MDS, was tailored for analysis of metal-coordinated proteins, as is the case of HDAC8. reMoDA integrates GROMACS [55–57], MDTraj [66] and other standalone tools—e.g. DSSP [67] and TMscore [68]— to compute a variety of metrics from the trajectories. These metrics are used as inputs for three other analysis modules: Principal Component Analysis (PCA), clustering, and energy (not applied here), which together enable both global and local comparative analyses across simulated systems. The reference system in our analysis was the Zn^{2+}-bound one. Cutoff values of 0.1 nm and 0.075 nm were set for the clustering module to perform global and local (around a selected residue) analyses, respectively.

Analyses of the relevant conformations selected from the trajectories were performed using various standalone or online tools, including GROMACS [55–57], ProtSA [69,70] and APBS software suite [71].

3. Results

3.1. Influence of Zn^{2+} on expression and purification of HDAC8

SDS-PAGE analysis revealed that most of the protein was expressed in *E. coli* in the insoluble fraction, indicating that it was mainly expressed in inclusion bodies. Because HDAC8 is a zinc-dependent protein, expression was performed in culture medium supplemented with Zn^{2+} ($ZnCl_2$). Purification of HDAC8 was done both with a buffer supplemented with Zn^{2+} and with no Zn^{2+} added. We used analytical size exclusion chromatography to study the oligomeric profile of the purified protein sample. HDAC8 purified and stored with Zn^{2+} exhibited two populations with apparent molecular weight of 622 kDa and 202 kDa, whereas HDAC8 purified and stored without zinc showed two populations with apparent molecular weight of 127 kDa and 46 kDa (data not shown). Because HDAC8 is expected to have a molecular weight of 43 kDa, these two populations might correspond to an elongated dimeric (or trimeric) and a monomeric conformation, respectively. These results suggest that HDAC8 purification was better without Zn^{2+} supplementation, and that Zn^{2+} promotes HDAC8 oligomerization, a phenomenon observed in other zinc-dependent proteins. After immobilized metal affinity chromatography, the purity of HDAC8 was over 95 %.

3.2. Influence of Zn^{2+} on HDAC8 structural stability: spectroscopy

The biological activity of a given protein depends on its three-dimensional structure and the influence of physico-chemical factors (temperature, pH, ionic strength, solutes, etc.), which modulate its conformational and functional landscapes.

After purification, CD was employed to assess HDAC8 secondary and tertiary structure in the presence and absence of Zn^{2+}. In the far-UV region, where available information is related to the secondary structure content, the spectra exhibited two bands typical from β-sheet (centered around 208 nm) and from α-helix (centered around 222 nm). This observation is in agreement with the crystallographic structure previously obtained by X-ray diffraction (PDB ID: 1T67) [25,72]. Removal of zinc by addition of EDTA slightly reduced the secondary structure (Fig. 1a), but deconvolution of the spectra using CDNN software provided a similar 30 % α-helix percentage in both conformations [73]. This percentage can also be estimated from the ellipticity at 222 nm, according to the following expression [74]:

$$\alpha\% = \frac{-[\theta]_{222} + 3000}{39000} \tag{16}$$

where $[\theta]_{222}$ is the mean residue molar ellipticity (MRE) at 222 nm. With this equation similar percentages are obtained: 34 % and 33 % α-helix percentage for Zn^{2+}-bound and Zn^{2+}-free HDAC8, respectively.

Removal of Zn^{2+} resulted in lower stability (T_m of 44.3 ± 0.2 °C for Zn^{2+}-bound HDAC8 and T_m of 39.8 ± 0.3 °C for Zn^{2+}-free HDAC8), as shown in Fig. 1b. The reduction in stability was also evident in the lower enthalpy of unfolding in the absence of Zn^{2+} ($\Delta H(T_m)$ = 39 ± 2 kcal/

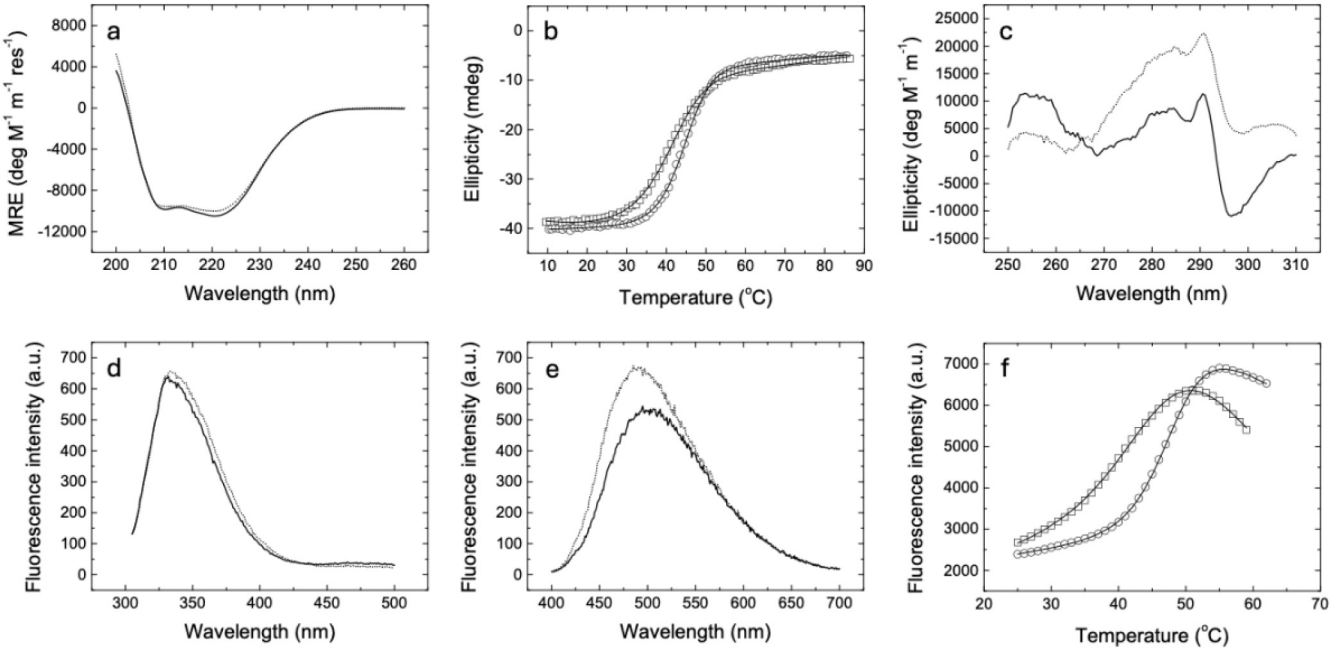

Fig. 1. Structural changes in HDAC8 upon Zn^{2+} removal observed by CD and fluorescence. (a) Far-UV CD spectra. Data from Zn^{2+}-free HDAC8 (dotted line) and Zn^{2+}-bound HDAC8 (continuous line) are shown. (b) Thermal unfolding assay followed by measuring ellipticity at 222 nm with a scanning rate of 1 °C/min. Data from Zn^{2+}-free HDAC8 (squares) and Zn^{2+}-bound HDAC8 (circles) are shown. Continuous lines correspond to the nonlinear least-squares fitting applying a single-transition unfolding model. (c) Near-UV CD spectra. Spectra were acquired in buffer 10 mM Tris/HCl pH 7, 20 mM KCl. Data from Zn^{2+}-free HDAC8 (dotted line) and Zn^{2+}-bound HDAC8 (continuous line) are shown. (d) Intrinsic tryptophan fluorescence emission spectra. Data from Zn^{2+}-free HDAC8 (dotted line) and Zn^{2+}-bound HDAC8 (continuous line) are shown. (e) Extrinsic ANS fluorescence emission spectra. Data from Zn^{2+}-free HDAC8 (dotted line) and Zn^{2+}-bound HDAC8 (continuous line) are shown. (f) Thermal unfolding assay followed by DSF (monitoring extrinsic SYPRO Orange fluorescence emission) with a scanning rate of 1 °C/min. Data from Zn^{2+}-free HDAC8 (squares) and Zn^{2+}-bound HDAC8 (circles) are shown. Continuous lines correspond to the nonlinear least-squares fitting applying a single-transition unfolding model. Assays were performed in triplicates.

mol) compared to that in the presence of Zn^{2+} ($\Delta H(T_m) = 58 \pm 3$ kcal/mol), which is reflected in a lower slope around the inflection point in the thermal unfolding curve (Fig. 1b). Therefore, Zn^{2+} dissociation caused a slight loss in secondary structure content and a considerably lower structural stability.

By analyzing the near-UV spectra, where the microenvironment surrounding the aromatic residues is probed, information on the tertiary structure is obtained. Each of the aromatic amino acids has a characteristic wavelength profile: tryptophans, with a peak close to 290 nm and fine structure between 290 and 305 nm; tyrosine, with a peak between 275 and 282 nm; and phenylalanine, with sharp fine structure between 255 and 270 nm [75]. Contrary to the results observed in the far-UV CD spectra, a notable difference was observed in the near-UV CD spectra with and without Zn^{2+} bound to HDAC8 (Fig. 1c), suggesting that removal of Zn^{2+} triggered a conformational change in which disposition of secondary structure motifs and the microenvironment of aromatic residues are different compared to the zinc-bound HDAC8. While the far-UV spectrum of a protein can be easily interpreted in terms of secondary structure features, the near-UV spectrum of a protein may not be readily amenable to detailed interpretation in terms of tertiary structure features. However, it represents a very useful "fingerprint" for the comparison of tertiary structures between native and non-native states of HDAC8. All these findings suggest, in accordance with the available crystallographic structures, that Zn^{2+} is required for the structural stability of HDAC8.

The main feature distinguishing HDAC8 from the other class I HDACs is the absence of a 50–111 amino acid C-terminal domain that extends from the catalytic domain [16]. The active site of HDAC8 consists of a long, narrow, hydrophobic tunnel at the end of which lies the catalytic machinery and the bound zinc ion. In order to study the changes elicited upon removal of the zinc ion, we added 100 μM EDTA and monitored the changes using fluorescence emission spectroscopy. Intrinsic fluorescence emission from tryptophans (Fig. 1d) and extrinsic fluorescence emission from the amphipathic probe 8-anilinonaphthalene-1-sulfonic acid (ANS) (Fig. 1e) were measured. HDAC8 contains four tryptophans and interpreting its fluorescence spectrum may be challenging. Nevertheless, a moderate redshift towards larger wavelengths can be observed upon Zn^{2+} removal (Fig. 1d), suggesting that the dissociation of Zn^{2+} triggers a slightly larger solvent-exposure of tryptophans in HDAC8 [76]. The extrinsic ANS fluorescence spectra were more informative as a reflection of the accompanying conformational change (Fig. 1e). A marked increase in intensity in the absence of Zn^{2+} and a blueshift was observed, suggesting that the Zn^{2+} dissociation results in enhanced binding of ANS molecules that experienced restricted mobility when associated with additional solvent-exposed hydrophobic surface in Zn^{2+}-free HDAC8.

Thermal stability assays were performed to evaluate HDAC8 stability using DSF (Fig. 1f). The fluorescence emission intensity of an external fluorescent probe (SYPRO Orange) was measured as a function of temperature, indirectly reporting the unfolding of HDAC8. The higher extrinsic fluorescence intensity observed in Zn^{2+}-free HDAC8 at low temperature, compared to Zn^{2+}-bound HDAC8, may reflect larger exposure of hydrophobic surface and binding of the dye to hydrophobic regions, in agreement with the observations based on ANS fluorescence. Removal of Zn^{2+} caused a reduction in stability, in reasonable agreement with the observations from CD: T_m of 47.9 ± 0.5 °C for Zn^{2+}-bound HDAC8 and T_m of 44.3 ± 0.5 °C for Zn^{2+}-free HDAC8, and $\Delta H(T_m)$ of 69 ± 4 kcal/mol for Zn^{2+}-bound HDAC8 and $\Delta H(T_m)$ of 41 ± 3 kcal/mol for Zn^{2+}-free HDAC8. The differences in the values observed in CD and DSF can be explained by the presence of the reporter dye which may act as a stabilizing ligand. Noteworthy, the reduction in the stability parameters caused by zinc dissociation is similar in both techniques.

In addition, isothermal chemical denaturation assays were performed to get an additional estimate of the protein stabilization energy

avoiding the uncertainty associated with extrapolating thermal unfolding results to lower temperatures (Fig. 2a). The linear extrapolation model for the effect of denaturant on protein stability provided quantitative estimates of the denaturant concentration at which 50 % unfolding occurs (2.5 M urea for Zn^{2+}-bound HDAC8, compared to 1.8 M urea for Zn^{2+}-free HDAC8) and the stabilization Gibbs energy for Zn^{2+}-bound and Zn^{2+}-free HDAC8 (5.2 ± 0.3 kcal/mol and 3.3 ± 0.2 kcal/mol at 20 °C, respectively) (Fig. 2a). In addition, the parameter m, which quantifies the susceptibility of the protein to the denaturant ($m = -\partial\Delta G/\partial[D]$) and scales fairly well with the change in solvent accessible surface area upon unfolding, is lower for the Zn^{2+}-free conformation (1.8 ± 0.2 kcal/mol M^{-1} and 2.1 ± 0.2 kcal/mol M^{-1} for Zn^{2+}-free and Zn^{2+}-bound conformations, respectively).

3.3. Influence of Zn^{2+} on HDAC8 structural stability: DSC

Thermal denaturations followed by circular dichroism (Fig. 1b) or fluorescence (Fig. 2c) might provide an incomplete description of the unfolding process undergone by HDAC8. DSC, considered the gold-standard for protein stability, was employed to assess the thermal stability of HDAC8 (Fig. 2b). After data collection, a preliminary model-free data analysis based on the van 't Hoff analysis provided first estimates of

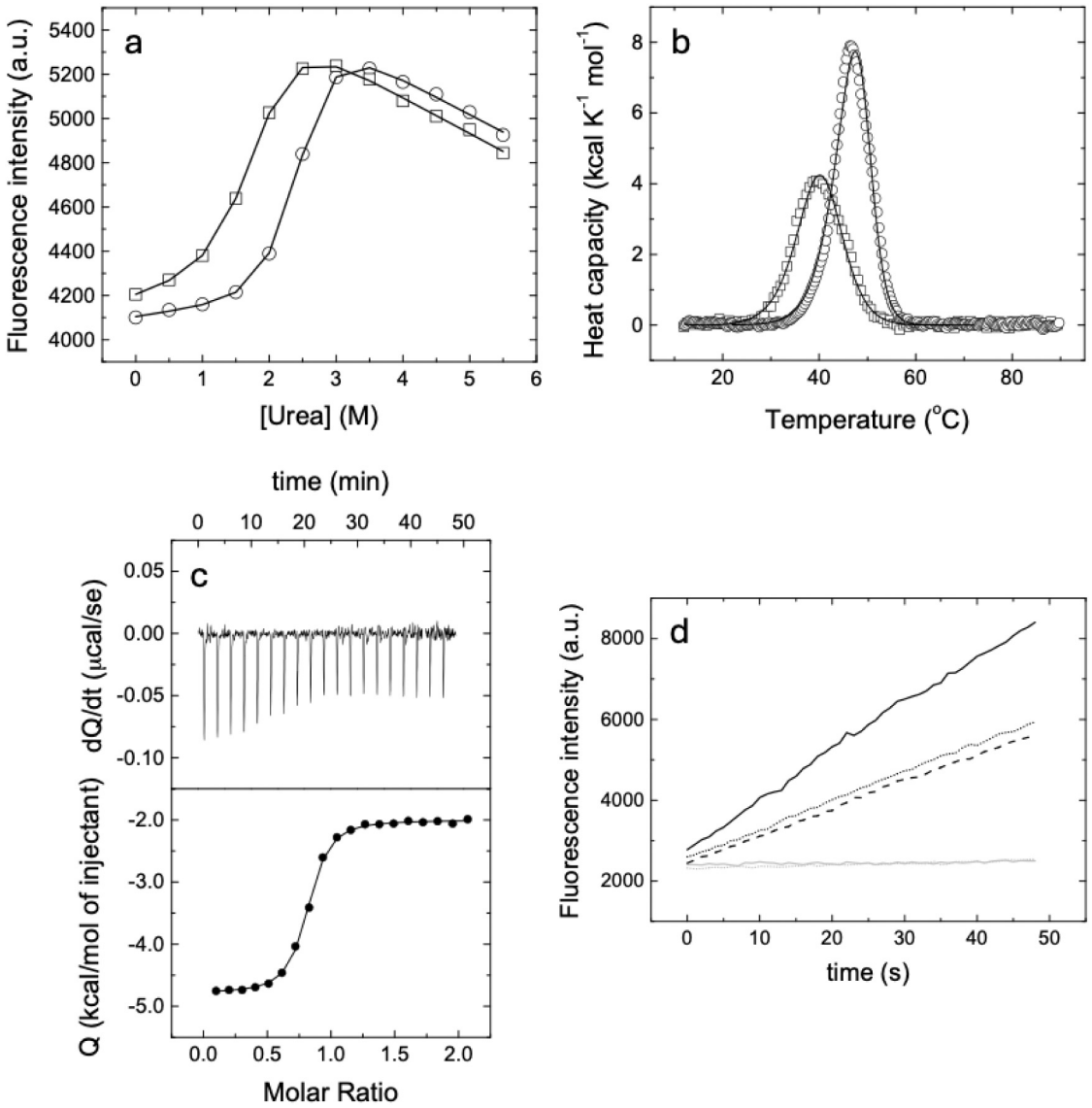

Fig. 2. Structural stability of HDAC8 assessed by chemical and thermal denaturation, interaction of HDAC8 with Zn^{2+}, and HDAC8 deacetylase activity. (a) Intrinsic tryptophan fluorescence emission at 340 nm measured as a function of urea concentration. Data from Zn^{2+}-free HDAC8 (open squares) and Zn^{2+}-bound HDAC8 (closed squares) are shown. Continuous lines correspond to the fitting employing correspond to the nonlinear least-squares fitting applying a single-transition unfolding model (Eq. (2)). (b) Thermal unfolding curves for Zn^{2+}-free HDAC8 (squares) and Zn^{2+}-bound HDAC8 (circles). For clarity, only 1 out of 10 data points is shown in the thermograms. The continuous lines correspond to the nonlinear least-squares fitting applying a single-transition unfolding model coupled to ligand (zinc) dissociation (Eqs. (5)–(9)). The Zn^{2+}-free HDAC8 unfolding is analyzed by imposing $[L]_T = 0$ in Eqs. (4)–(9). (c) The interaction of HDAC8 with Zn^{2+} was assessed by isothermal titration calorimetry. (Upper panel) Thermogram, showing the thermal power as a function of time. (Lowe panel) Binding isotherm showing the ligand-normalized heat effect per injection as a function of the molar ratio. Nonlinear least-squares regression data analysis (continuous line) provided an estimation of the affinity, enthalpy, and stoichiometry of the interaction. (d) Time evolution of fluorescence emission at 460 nm, with excitation at 390 nm, after adding 20 µM substrate to 0.2 µM enzyme. Fluorescence emission increase reflects the coupled processing (deacetylation) of the peptide substrate by HDAC8 and a protease resulting in a free fluorogenic 7-amino-4-methylcoumarin (AMC) moiety. Data from Zn^{2+}-free HDAC8 (black dotted line) and Zn^{2+}-bound HDAC8 (black continuous line) are shown, together with trichostatin A-inhibited HDAC8 (Zn^{2+}-free enzyme, gray dotted line; Zn^{2+}c-bound enzyme, gray continuous line). In addition, the activity of Zn^{2+}-free HDAC8 with 5 mM EDTA added is also shown (black dashed line). Assays were performed in triplicates.

the stability parameters and allowed selecting the appropriate unfolding model. Removal of Zn^{2+} by addition of EDTA resulted in a lower stability (T_m of 46.5 ± 0.2 °C for Zn^{2+}-bound HDAC8 and T_m of 39.8 ± 0.2 °C for Zn^{2+}-free HDAC8, estimated from the temperature of the maximal heat capacity), as shown in Fig. 4. The reduction in stability was also evident in the lower calorimetric enthalpy of unfolding in the absence of Zn^{2+} ($\Delta H(T_m)$ of 72 ± 3 kcal/mol for Zn^{2+}-bound HDAC8, and $\Delta H(T_m)$ of 54 ± 2 kcal/mol for Zn^{2+}-free HDAC8, estimated from the area under the concentration-normalized unfolding curve). These model-free stability parameters are in reasonable agreement with those obtained from spectroscopy (CD and DSF). Using Eq. (3), the van 't Hoff enthalpy was calculated in both cases: 90 ± 3 kcal/mol for Zn^{2+}-bound HDAC8, and 59 kcal/mol for Zn^{2+}-free HDAC8. And the ratio between the van 't Hoff enthalpy and the calorimetric enthalpy was also calculated: 1.10 ± 0.05 for Zn^{2+}-bound HDAC8, and 1.26 ± 0.06 for Zn^{2+}-free HDAC8. According to these ratios, the single transition model was the appropriate model for analyzing the data.

The single transition model applied to the Zn^{2+}-free HDAC8 provided the following stability parameters: T_m = 38.4 ± 0.2 °C, and $\Delta H(T_m)$ = 55 ± 2 kcal/mol, whereas the same model applied to the Zn^{2+}-bound HDAC8 provided the following stability parameters: T_m = 45.8 ± 0.2 °C, and $\Delta H(T_m)$ = 77 ± 3 kcal/mol. These values are slightly different to the ones obtained in the model-free analysis because of the gross estimation performed in that preliminary analysis. It should be remembered that the temperature of the inflection point (maximum slope) in spectroscopy and the temperature for the maximum heat capacity in DSC are close but do not coincide with the real T_m; in fact, the real T_m is slightly lower than those two temperatures [77].

The unfolding of the Zn^{2+}-bound protein has been analyzed overlooking the presence of Zn^{2+} that will dissociate from the protein as the unfolding process takes place. Thus, it has been considered that Zn^{2+} is an "environmental" element that simply modulates the stability parameters. However, the unfolding of the Zn^{2+}-bound HDAC8 must be analyzed considering the coupling between the conformational and ligand binding equilibrium (Eqs. (4)–(9)). Performing this analysis by fixing the intrinsic stability parameters for HDAC8 in the absence of Zn^{2+}, the binding constant and the binding enthalpy at 25 °C could be estimated from the fitting of the Zn^{2+}-bound HDAC8 unfolding curve (i.e., from the stabilization effect induced by Zn^{2+} binding): K_B = 3.3 ± 0.7·10^7 M^{-1} (K_d = 0.030 ± 0.006 μM), and ΔH_B = −3.6 ± 0.5 kcal/mol (Fig. 2b).

3.4. Interaction of HDAC8 with Zn^{2+}: ITC

The thermodynamic parameters for the interaction of HDAC8 with its zinc cofactor were estimated by ITC, the gold-standard for the characterization of biomolecular interactions (Fig. 2c) [78]. The binding isotherm was constructed from the thermogram after baseline correction and normalizing the heat effect per injection with the amount of ligand injected. Applying the single binding site model to the binding isotherm, a binding constant K_B of 1.2 ± 0.2·10^7 M^{-1} (K_d = 0.08 ± 0.01 μM), and a binding enthalpy ΔH_B of −2.8 ± 0.3 kcal/mol at 25 °C were estimated. The apparent stoichiometry n was 0.82 ± 0.03, indicating that about 80 % of the protein in the cell was binding-competent (the stoichiometry 1:1 is implicitly considered in the model; therefore, the fractional value of n is used to normalize the concentration of active protein). The interaction parameters estimated by ITC are in very good agreement with those estimated from DSC.

3.5. Influence of Zn^{2+} on HDAC8 activity

To test the influence of the presence of Zn^{2+} on the deacetylase activity of HDAC8, the enzymatic activity of the enzyme was assessed for the Zn^{2+}-bound conformation and for the Zn^{2+}-free conformation (Fig. 2d). The negative controls (the enzyme incubated with the known HDAC8 inhibitor trichostatin A, or no enzyme added to substrate) provided a flat time evolution of the signal corresponding to zero activity level, whereas the Zn^{2+}-bound HDAC8 exhibited a non-zero signal as expected. Interestingly, the Zn^{2+}-free HDAC8 showed an intermediate non-zero signal, significantly lower than that of the Zn^{2+}-bound enzyme but larger than that of the controls (added HDAC8 inhibitor or no enzyme added). This residual activity of HDAC8 without Zn^{2+} may be due to the composition of the commercial kit buffer (which could contain metal ions) or to the fact that inhibition of the protein with an inhibitor targeting the Zn^{2+} binding site may have a different outcome compared to Zn^{2+} removal with EDTA (which could be influenced by the kinetics of Zn^{2+} interaction with HDAC8 and EDTA, or the Zn^{2+}-free enzyme could have some residual activity).

3.6. Influence of Zn^{2+} on HDAC8 structural stability: MDS

The tailored Python-based workflow, reMoDA, enabled us to perform a variety of comparative multi-replica analyses on the 5-μs molecular dynamics trajectories of the Zn^{2+}-bound and Zn^{2+}-free systems —both at the whole-structure level and locally. For global structure comparative analysis, the multiparametric module generated a variety of plots (Fig. 3), including: root mean square deviation (RMSD), radius of gyration (Rg), TMscore, fraction of native contacts, root mean square fluctuation (RMSF), alpha+beta (α + β) secondary structure, coil structure, intraprotein and protein-water hydrogen bonds, and solvent-accessible surface area (SASA). From the comparative panels in Fig. 3, the most prominent differences between the Zn^{2+}-bound (upper plots in panels) and Zn^{2+}-free (lower plots in panels) systems are captured by the following parameters: TMscore (lower in Zn^{2+}-free replicas, panel c), fraction of native contacts (lower in Zn^{2+}-free, panel d), α + β secondary structure (lower in Zn^{2+}-free, panel g), coil structure (higher in Zn^{2+}-free, panel f), intraprotein H-bonds (lower in Zn^{2+}-free, panel h), protein-water H-bonds (higher in Zn^{2+}-free, panel i), and SASA (higher in Zn^{2+}-free, panel j).

The PCA module of our customized version of reMoDA generated a time series of PC1 vs. PC2 plots (100 intervals of 50 ns each) for the entire systems (global analysis), based on the parameters extracted from the 5-μs trajectories using the multiparametric core module. A representative subset of these PCA plots is shown in Fig. 4a, highlighting two key observations: (1) a progressive and well-defined separation between the two systems over time, despite both starting from a common conformation (see the 0–50 ns interval); and (2) a tighter grouping of the Zn^{2+}-bound replicas in contrast to the broader dispersion observed for the Zn^{2+}-free replicas. A video integrating the 100 plots generated at 50 ns intervals was produced and is provided as Supporting information.

Moreover, the 2D-RMSD-based clustering module of reMoDA enabled an additional comparison focused exclusively on structural evolution over time between pairs of replicas from the simulated systems. Fig. 4b, presents three representative clustering evolution plots, each comparing one Zn^{2+}-bound replica with a Zn^{2+}-free replica. Consistent with the PCA results discussed above, this analysis reveals two key findings: (1) the trajectories of the systems diverge structurally over time, with no overlapping clusters observed at any point; and (2) the Zn^{2+}-bound replicas adopt significantly fewer distinct structural clusters compared to the Zn^{2+}-free replicas, based on the 0.1 nm cutoff used for clustering.

This clustering analysis allowed the selection of representative conformations from both the Zn^{2+}-bound and Zn^{2+}-free trajectories for further analyses. Specifically, one conformation was extracted from each structural cluster that persisted for at least 250 ns. Following this criterion, 6 and 8 representative conformations were selected for the Zn^{2+}-bound and Zn^{2+}-free systems, respectively (Fig. 4c). Structural alignment between conformations within each system revealed maximum pairwise Cα-RMSD values of 0.3 nm for the Zn^{2+}-bound system and 0.55 nm for the Zn^{2+}-free system. These values further support that the Zn^{2+}-bound system largely retained its initial conformation over the simulated time, while the Zn^{2+}-free system underwent substantial

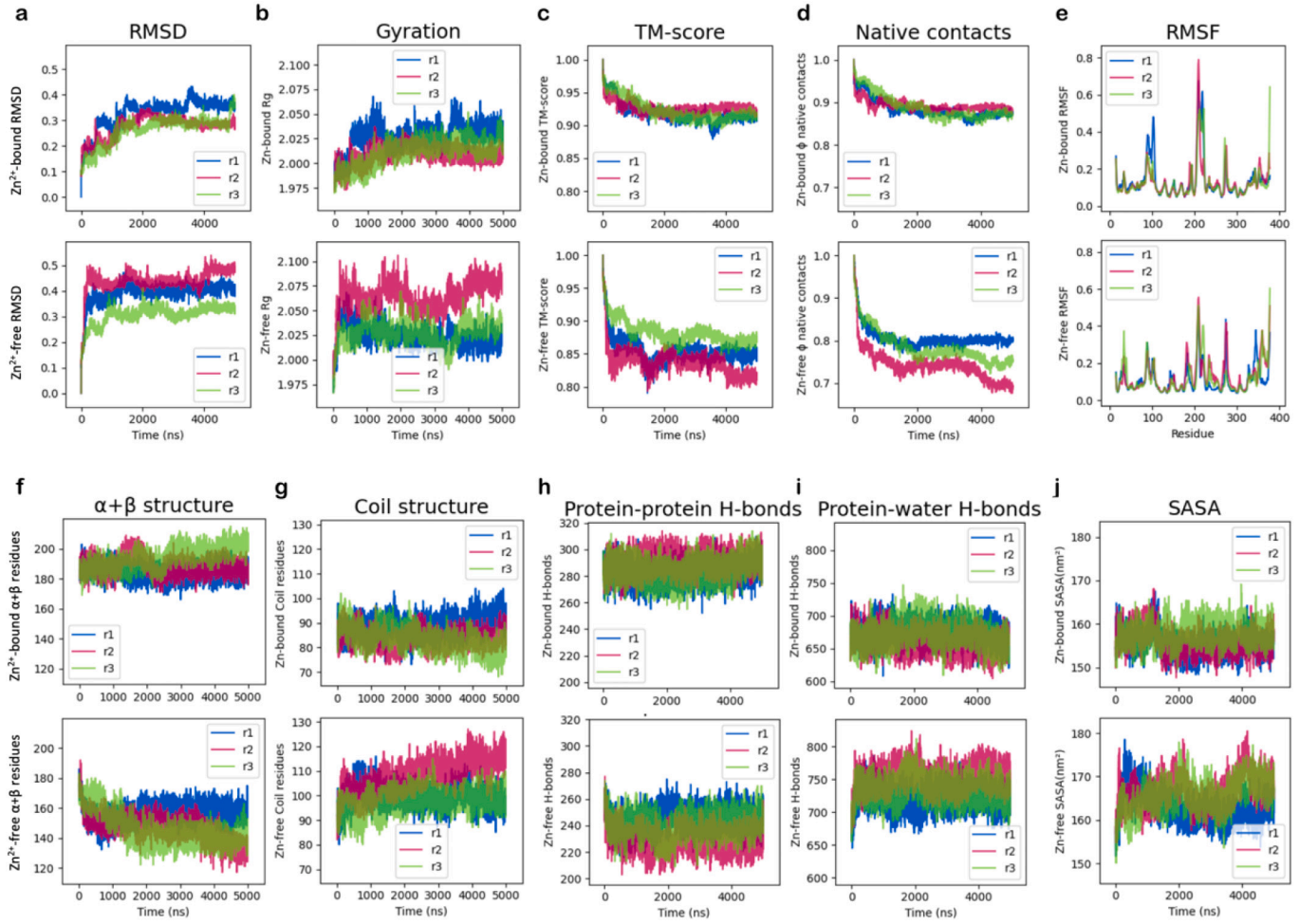

Fig. 3. Comparative multi-replica, multiparametric analysis of MD trajectories obtained from the reMoDA workflow. Each panel shows an upper plot for the three Zn^{2+}-bound trajectory replicas and a lower plot for the three Zn^{2+}-free replicas. Time plots are shown for: (a) RMSD, (b) radius of gyration, (c) TMscore, (d) fraction of native contacts, (f) α + β secondary structure, (g) coil structure, (h) intraprotein H-bonds, (i) protein-water H-bonds, and (j) SASA. (e) Per-residue RMSF plot. The initial frame (time = 0) of each trajectory was used as the reference structure for RMSD, TMscore, fraction of native contacts and RMSF calculations. The color scheme for the replicas is indicated in the legends of each panel.

conformational changes. In alignment with this, residue pairwise connectivity matrixes obtained for all pairs of simulated replicas, from both Zn^{2+}-bound and Zn^{2+}-free systems (Fig. S1), revealed that the number of common residue-residue interactions (i.e., interactions present in both compared HDAC8 conformations) is significantly lower in Zn^{2+}-bound vs. Zn^{2+}-free comparisons than in Zn^{2+}-bound vs. Zn^{2+}-bound or even in Zn^{2+}-free vs. Zn^{2+}-free comparisons.

One of the main structural variations observed in the Zn^{2+}-free replicas occurs around the catalytic site (see the Zn^{2+}-bound vs. Zn^{2+}-free structural alignment in Fig. 4c). The removal of Zn^{2+} in HDAC8 results in increased flexibility and rearrangement of several loops (e.g., D176-G182, H201-G220, Q263-T280, G341-E358) that define the active site and partially shape the long, narrow hydrophobic tunnel leading into it. A partial collapse of this tunnel in the Zn^{2+}-free system is evident in the comparative surface representations shown in Fig. S2a. Comparative Ramachandran plots for backbone φ vs. ψ angles and side-chain χ1 vs. χ2 angles of amino acids D178, H180 and D267 —typically involved in Zn^{2+} coordination in holo-HDACs (Fig. 4c)— also illustrate the significant conformational differences exhibited in this region.

Another observed feature is the reduced secondary structure content (~20–30 %) in Zn^{2+}-free compared to Zn^{2+}-bound HDAC8 (see Figs. 3f and 4c). On the one hand, the partial or complete loss of the last helix (P359–H375) in the Zn^{2+}-free systems appears to be partially offset by the sporadic de novo formation of small α-helices within flexible loops, as well as by the transient elongation of certain pre-existing helices. On the other, the shortening of several β-strands forming the central β-sheet is also observed (Fig. 4c). Altogether, these findings are consistent with the reduced overall secondary structure content observed in our CD measurements, as well as with the comparable α-helix content detected in both HDAC8 systems.

Further differences between these systems are captured from solvent-accessible surface area (SASA, as calculated by ProtSA server [69,70]) and electrostatic potential surfaces (EPS, as calculated by APBS software [71]). Average total, polar, and apolar solvent-accessible surface areas (SASA) were significantly lower in Zn^{2+}-bound conformations compared to Zn^{2+}-free ones (Fig. S3). Moreover, Zn^{2+}-free conformations exhibited more pronounced (larger areas) negative electrostatic potentials (EPS) on the surface facing the active site, compared to their Zn^{2+}-bound counterparts (Fig. S4).

To further evaluate the structural changes occurring around the active site upon Zn^{2+} removal, the local analysis modes of the comparative multiparametric and PCA modules from the customized reMoDA workflow were applied to residues L179 (Fig. S5), A266 (Fig. S6) and T268 (Fig. S7) on the simulated trajectories. Comparative time plots for intraprotein and protein-water hydrogen bonds, fraction of native contacts, and solvent-accessible surface area (SASA) (panels a) were generated, and the resulting data were used as input for the PCA shown in panels b. The PCA plots —for all three residues— clearly

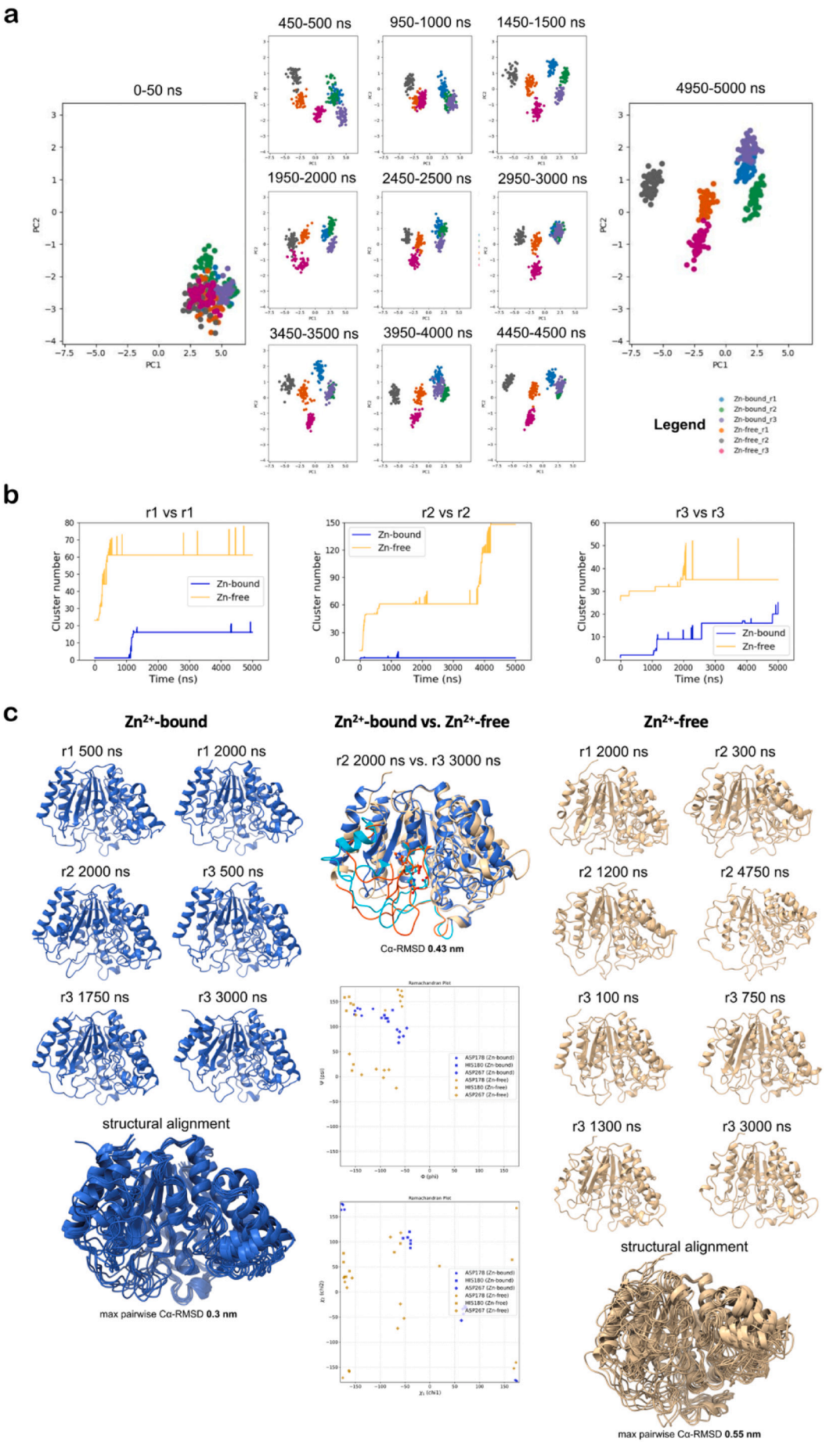

(caption on next page)

Fig. 4. Multi-replicate analysis of the conformational evolution of Zn^{2+}-bound and Zn^{2+}-free HDAC8 structures over the course of molecular dynamics trajectories. (a) Representation of a selection of eleven 50-ns interval plots along the simulated time, each displaying the first two principal components (PC1: x-axis, PC2: y-axis) of the PCA performed for the six simulated replicas (three per system). Each dot of a given replica represents a frame of its simulated trajectory within the time interval. The time interval of each plot is shown on the top. The color scheme is indicated in the legend located at the bottom right. (b) Representation of three compared clustering (2D-RMSD-based) plots among all the possible replicas pairings for the simulated Zn^{2+}-bound and Zn^{2+}-free systems. Each plot shows the temporal evolution of structural clusters identified for the compared systems. The color scheme is indicated in the insets displayed within each plot. (c) Representative conformations (shown in cartoon representation) selected from the structural clusters shown in (b), each corresponding to a cluster that persisted for at least 250 ns along the simulated trajectories. Structural alignments of all selected conformations are shown for both for Zn^{2+}-bound and Zn^{2+}-free systems. A pairwise overlap between one representative conformation from each system is shown in the middle column at the top. HDAC8 loops in the vicinity of the active site (D176–G182, H201–G220, Q263–T280, G341–E358), which exhibit an increased flexibility and rearrangement, are highlighted in cyan (Zn^{2+}-bound) and red (Zn^{2+}-free) to facilitate comparison. Residues D178, H180, and D267 —involved in Zn^{2+} coordination in holo-HDAC8— are depicted as balls and sticks. Ramachandran plots of backbone φ vs. ψ angles and side-chain χ_1 vs. χ_2 angles for these residues, obtained using the gmx rama tool from GROMACS, are provided in the middle column at the bottom. The color scheme, consistent with that used for the representative conformations, is indicated in the legends within the plots.

indicate that the active site of Zn^{2+}-free HDAC8 undergoes substantial conformational changes compared to the well-preserved conformation observed in the Zn^{2+}-bound systems. It has been previously reported that HDAC8 shows considerable flexibility around the metal binding site [16,79]. Thus, the vicinity of the active site is malleable and able to accommodate different (substrates and inhibitors), and deacetylate lysines in different structural contexts. In particular, L1 and L2 loops surrounding the metal binding site are highly dynamic. However, in these references it has been reported that residues located near the metal binding site, e.g., Y100 and D101, show a highly conserved structural configuration. In our case we have focused on other residues even closer to the metal binding site (L179, A266, and T268), for which we observed a highly conserved configuration in Zn^{2+}-bound HDAC8 during the simulations, whereas they are quite dynamic in Zn^{2+}-free HDAC8.

To evaluate whether the microenvironments of tryptophan residues were also affected in silico —i.e., throughout the MD simulations— local analyses using the reMoDA workflow were also performed for the four tryptophans present in HDAC8: W137, W141, W294, and W315 (Figs. S8–S11). The PCA results (panel b) clearly reveal local differences in the microenvironments of Trp residues following Zn^{2+} removal, in good agreement with the data obtained from our near-UV CD experiments.

4. Discussion

Approximately 10 % of human proteins are zinc-dependent proteins [31,32]. Therefore, it is relevant to understand how the Zn^{2+} cofactor modulates their structural stability, besides the possible catalytic role it may have. Zn^{2+} is required for stability, as it provides a substantial amount of stabilization Gibbs energy through the direct interaction within the coordination cage in the binding sites, but also indirectly at distant sites that may become rearranged upon Zn^{2+} binding. Furthermore, in some zinc-binding proteins the cofactor exerts an essential catalytic role. NS3 protease from the hepatitis C virus is an example of a zinc-dependent enzyme in which the zinc cofactor is only required for structural stabilization [43], whereas carbonic-anhydrase is an example of a zinc-dependent enzyme in which the zinc cofactor is required for structural stabilization and catalytic activity [80].

The abundance of zinc-dependent proteins in prokaryotes and eukaryotes makes them important pharmacological targets at a time when there is an urgent need to find new drugs for neglected diseases, emerging diseases, or diseases with no effective therapies. Thus, new action mechanisms are sought for known or new targets in order to develop complementary therapies that broaden the spectrum of application. By studying the conformational and functional landscape of a protein, relevant conformational and functional states can be identified and employed as targets for drug discovery. In this work, we have focused on the thermodynamic characterization of the conformational and Zn^{2+} binding equilibria of HDAC8, a protein target associated with certain types of cancer and neurological diseases. The aim was to prove that this protein populates an alternative, inactive conformational state in the absence of Zn^{2+} which is physiologically relevant and could be targeted for developing allosteric inhibitors.

Expression of HDAC8 in *E. coli* was improved when cultures were supplemented with Zn^{2+}, but its purification yield was much higher with no Zn^{2+} supplementation. Therefore, although Zn^{2+} is a required cofactor for stability and activity, high Zn^{2+} concentrations can be harmful, resulting in protein aggregation. This phenomenon has been observed in other zinc-dependent proteins [42,81,82].

The spectroscopic and calorimetric results for HDAC8 can be summarized as follows: 1) removal of Zn^{2+} hardly alters the secondary structure content (far-UV CD), but it causes a considerable change in tertiary structure and increases the exposure of hydrophobic surface to the solvent (near-UV CD and fluorescence); and 2) removal of Zn^{2+} lowers the thermal and chemical stability (far-UV CD, fluorescence, and DSC): T_m decreases in 4–7 °C and $\Delta H(T_m)$ decreases by 30–40 %.

The preliminary model-free analysis of the DSC data provided a ratio between the van 't Hoff enthalpy and the calorimetric enthalpy of 1.10 for Zn^{2+}-free HDAC8 and 1.26 for Zn^{2+}-bound HDAC8. While the first value is reasonably close to 1, corresponding to a two-state (single transition) unfolding process, the second would indicate that the molecular events underlying the unfolding process would be more complex. In fact, when a protein bound to a ligand undergoes unfolding, the ratio of the enthalpies is very often larger than 1 because there is a significant contribution to the overall observed unfolding enthalpy from the ligand dissociation (larger area of the unfolding curve) and the increase in stability is accompanied by an apparent increase in unfolding cooperative (narrower unfolding transition).

The binding parameters for the interaction of HDAC8 with Zn^{2+} have been obtained directly from ITC, but they have also been estimated from the thermal unfolding of the Zn^{2+}-bound HDAC8 by applying a model in which the coupling between the conformational and the zinc binding equilibria is explicitly considered and solved with no approximations. The Zn^{2+}-bound HDAC8 corresponds to the so-called "holoenzyme" or "holoprotein". However, that situation should not be treated as a "protein" different from the "apoprotein" (ligand-free HDAC8), but rather as the "apoprotein" in the presence of an interacting ligand. This approach complicates the data analysis, but it provides further insights and facilitates the interpretation of the results.

The mathematical approach in which the coupling between the conformational and the Zn^{2+} binding equilibria are explicitly considered (Eqs. (4)–(9)) provides further insight into the stabilizing effect of Zn^{2+} on HDAC8 and strengthen the parameter estimation and the conclusions drawn. This formalism explicitly accounts for the populations of the native (P_N), ligand-bound native (P_{NL}), and unfolded (P_U) states, from which the Gibbs energy difference between the unfolded state and the (ligand-free and ligand-bound) native states can be calculated:

$$\Delta G(T,[L]) = -RT\ln\frac{K(T)}{1+K_B(T)[L]} = -RT\ln\frac{P_U(T,[L])}{P_N(T,[L])+P_{NL}(T,[L])} \quad (17)$$

which is a function of the temperature and the concentration of free ligand (Zn^{2+} in this case). By plotting this quantity for HDAC8 as a function of the temperature for several concentrations of Zn^{2+}, it can be seen that Zn^{2+} binding accounts for 50 % of the overall stabilization

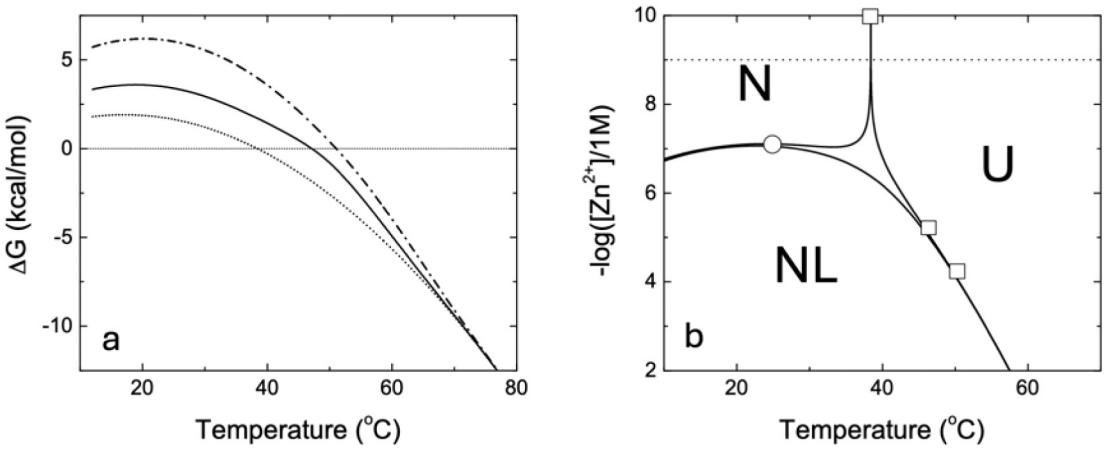

Fig. 5. Dissection of the contribution of Zn^{2+} binding to the structural stability of HDAC8 and temperature-concentration phase diagram. (a) Apparent Gibbs energy of stabilization (Eq. (17)) as a function of temperature for 10 μM HDAC8 in the presence of 0 μM (dotted line), 10 μM (continuous line), and 60 μM (dashed-dotted line) total concentration of Zn^{2+}. The intercept of the apparent stability Gibbs energy with the x-axis (i.e., the temperature for which ΔG is zero corresponds to the observed T_m): 38.4, 47.1, and 51.0 °C for 0, 10, and 60 μM total concentration of Zn^{2+}, respectively. Additional experiments performed by adding 50 μM Zn^{2+} to Zn^{2+}-bound HDAC8 provided a T_m of 50.3 °C (data not shown), which is close to the estimated value of 51 °C from this plot (60 μM total Zn^{2+}, dashed-dotted line). (b) Temperature-ligand concentration phase diagram of HDAC8 showing the coexistence lines (a given state is 50 % populated) and the regions where the population of each conformational state is greater than 50 %, together with a "triple point" in which the three states are similarly populated. The circle corresponds to the Zn^{2+} binding affinity ($logK_B = -logK_d$) at 25 °C experimentally determined by ITC, and the squares correspond to the unfolding temperatures at the different Zn^{2+} concentrations: 38.4, 47.1, and 51.0 °C for 0, 10, and 60 μM total concentration of Zn^{2+}c, experimentally determined by DSC. The dotted line corresponds to a concentration of free Zn^{2+} of 1 nM, which is an upper bound for the intracellular free concentration.

energy for Zn^{2+}-bound HDAC8 (Fig. 5A): at 20 °C, the stabilization Gibbs energy of Zn^{2+}-free HDAC8 is 1.9 ± 0.2 kcal/mol, whereas the stabilization Gibbs energy of Zn^{2+}-bound HDAC8 is 3.6 ± 0.3 kcal/mol. Furthermore, the stabilization Gibbs energy of Zn^{2+}-bound HDAC8 with an additional 50 μM Zn^{2+} is 6.2 ± 0.3 kcal/mol at 20 °C, but the induced increase in T_m is very modest compared to the difference between Zn^{2+}-free and Zn^{2+}-bound HDAC8 with just 10 μM total Zn^{2+} concentration difference. Interestingly, the chemical denaturation experiments were performed at 20 °C, and they provided very similar stabilization Gibbs energies: 3.3 kcal/mol for Zn^{2+}-free HDAC8 and 5.2 kcal/mol for Zn^{2+}-bound HDAC8, resulting in a difference of 1.9 kcal/mol at 20 °C, compared to an estimated difference of 1.7 kcal/mol at 20 °C from the DSC experiments (Fig. 5A).

The thermodynamic parameters for the stability of HDAC8 and its interaction with Zn^{2+} can be used to construct the temperature-[ligand] phase diagram of the protein [83,84], providing a quantitative depiction of the conformational landscape showing the relevant accessible states: Zn^{2+}-free native state, N; Zn^{2+}-bound native state, NL; and unfolded state, U (Fig. 5B). The coexistence line where NL is 50 % populated corresponds to the temperature dependence of the apparent Zn^{2+} binding constant $logK_B^{app}$, and the coexistence line where U is 50 % populated corresponds to the Zn^{2+} concentration dependence of the apparent T_m. At free Zn^{2+} concentrations below 1 nM and around 37 °C, Zn^{2+}-free HDAC8 and unfolded HDAC8 are the only significantly populated conformational states, with a Zn^{2+}-bound HDAC8 population much lower than 1 % (Fig. 5B), supporting the idea of a physiologically relevant Zn^{2+}-free HDAC8. Very likely, a crowded intracellular environment and the presence of accessory proteins acting as metal chaperones serving as zinc reservoirs or dedicated to the transport and delivery of zinc to the active site of enzymes, together with the energy barrier associated with the dissociation of Zn^{2+}, may help in shifting the equilibrium towards the Zn^{2+}-bound state [85,86].

A comprehensive computational study of the conformational features of HDAC8 in the Zn^{2+}-free and the Zn^{2+}-bound states has been accomplished through 5-μs replicas of MD simulation trajectories. The parameterization of the Zn^{2+}-bound active site of the enzyme represented the initial modeling step for the subsequent analysis. Overall, this detailed structural analysis revealed that the removal of the Zn^{2+} cofactor elicited considerable structural changes indicating a loss in structural integrity (Fig. 3): lower TMscore, lower number of native contacts, lower percentages of secondary structure, larger percentage of coil structure, lower number of intraprotein hydrogen bonds and larger number of protein-water hydrogen bonds, and larger solvent-accessible surface area. All these findings are in agreement with the experimental observations: lower molar residue ellipticity at 222 nm, higher level of ANS binding, lower unfolding temperature and enthalpy, lower susceptibility to denaturant in chemical denaturation, and lower stability Gibbs energy in thermal and chemical denaturation.

The set of MD simulation replicas allowed exploring conformational propensities through time series and taking representative conformations at different time points. While Zn^{2+}-bound conformations always clustered very closely according to the PCA analysis, Zn^{2+}-free conformations showed dispersion and wider variability, reflecting the heterogeneity of the Zn^{2+}-free conformational state (Fig. 4 and SI figures). PCA analysis allowed representative conformations to be established as a function of Zn^{2+} binding site occupancy, with an RMSD of 0.3 nm for the Zn^{2+}-bound state and 0.55 nm for the Zn^{2+}-free state (Fig. 4). Zn^{2+} removal resulted in a significant level of rearrangement that affected the residues around the catalytic site and the particular configuration of residues involved in catalysis (D178, H180 and D267), as well as the partial collapse of the hydrophobic tunnel leading to the catalytic site (Figs. 4 and S2). Interestingly, regions away from the Zn^{2+} binding site showed a marked level of disorder and an order-disorder transition upon Zn^{2+} removal. This phenomenon was particularly important in the C-terminal domain, where a large portion containing the last α-helix undergoes extensive destabilization (Fig. 4). The cofactor zinc is essential for the catalytic activity of HDAC8 because it is involved in the catalytic mechanism. Moreover, the observations described here represent an interesting example of allosteric regulation in which ligand binding, in addition to controlling protein activity, governs the conformation of the entire protein molecule: ligand binding/dissociation at a particular site affects distant regions of the molecule, which may have functional implications beyond the catalytic activity (e.g., interaction with other biological partners).

According to previous works, although HDAC8 was originally described as a zinc-dependent enzyme, other metals (such as cobalt,

manganese, iron, and nickel) bind to HDAC8 and modulate its catalytic activity and the inhibitory potency of competitive inhibitors [17,87,88]. The catalytic of HDAC8-catalyzed deacetylation depends on the identity of the divalent metal bound to the active site, being Fe^{2+}-HDAC8 more active than Zn^{2+}-HDAC8. In addition, the binding affinity of Zn^{2+} interacting with HDAC8 is several orders of magnitude higher than that of Fe^{2+}, and the intracellular concentration of free Zn^{2+} is also several orders of magnitude lower than that of Fe^{2+}. Consequently, it has been hypothesized that HDAC8 may utilize a different metal under different conditions in vivo. However, even though we agree that other metals, in particular Fe^{2+}, would be more relevant for HDAC8, we selected Zn^{2+} based on: 1) HDAC8 was initially identified as a Zn^{2+}-binding protein; 2) Zn^{2+} may serve as a prototypical metal for HDAC8 for assessing the influence of metal binding on its conformational features and its conformational landscape; and 3) Zn^{2+} is easier to work with than Fe^{2+} in solution. Most of results observed for HDAC8 with Zn^{2+} in our manuscript (e.g., physiological relevance of Zn^{2+}-free native state, or Zn^{2+}-free HDAC8 as a drug target) could be extrapolated to other metals, and using Zn^{2+} as a prototypical metal for HDAC8 does not invalidate our conclusions. Other free cations, such as Fe^{2+}, Co^{2+}, Ni^{2+}, Mn^{2+}, or Zn^{2+} will be at very low free concentrations inside the cell, and therefore, the population of metal-free HDAC8 will be significant under physiological conditions.

5. Conclusions

HDAC8 is a zinc-dependent protein with a conformational landscape modulated by its interaction with Zn^{2+}. Thus, HDAC8 represents an interesting example of an allosteric protein, in the broad sense, in which its zinc cofactor modulates its conformational equilibrium. In this work we have provided a comprehensive experimental and computational characterization of the conformational equilibrium and its modulation by the interaction with Zn^{2+}. HDAC8 must be under considerable stress inside the cell, as the structural stability of the protein is low and the intracellular concentration of free Zn^{2+} is very low. Cellular crowding, metal chaperones, and the presence of other metals (e.g., Fe^{2+}) can help alleviate stress by shifting the equilibrium towards the Zn^{2+}-bound (or metal-bound) state, but the Zn^{2+}-free inactive state and the unfolded state remain major actors in the conformational landscape. Thus, inactive states (e.g., Zn^{2+}-free native protein and Zn^{2+}-free unfolded protein) are physiologically relevant and they may be specifically targeted for drug discovery.

We do not suggest that zinc-free HDAC8 exerts any physiological function. On the contrary, according to current knowledge and our experimental data, zinc-free HDAC8 is inactive, as it is unable to remove acetyl groups from histones and other target proteins. The zinc-free conformation is considerably different from the zinc-bound conformation, according to the experimental evidence collected in the manuscript. We use the term “relevant” in a statistical and quantitative sense, rather than a functional one. Given the extremely low intracellular concentration of free zinc, a substantial portion of HDAC8 is expected to exist without zinc cofactor under physiological conditions. Therefore, the relevance stems from the large, predicted population of functionally inactive protein in the cell. The absence of activity in zinc-free HDAC8 is relevant under normal physiological conditions, as the extremely low intracellular concentration of zinc results in a considerable percentage of HDAC8 lacking the zinc cofactor.

The lack of a well-defined structure in a protein does not prevent it from being druggable and being considered as a drug target. In fact, intrinsically disordered proteins can be targeted with small molecules that modulate their function. NUPR1, a protein associated with pancreatic cancer, is one of the first completely unfolded proteins proven to be targeted with drugs: we have been able to identify low molecular weight compounds with the ability to bind to NUPR1, inhibit protein-protein interactions involving NUPR1, and reduce the growth of, or even eliminate, pancreatic adenocarcinomas xenografted in mice [89–91].

We have also identified small molecules that bind and inhibit the activity of conditionally disordered proteins (proteins that adopt different conformations depending on environmental conditions, such as cofactor availability). The NS3 protease from the hepatitis C virus and the BFT-3 enterotoxin form *B. fragilis* are two zinc-dependent proteins that, in the absence of zinc, adopt a partially unfolded and inactive conformation. Previously, we reported on several small molecules that inhibit the activity of NS3 protease and BFT-3 in cell assays [92]. These molecules interact with the partially unfolded, inactive, zinc-free conformation of both targets through an allosteric mechanism. In particular, we have shown that several compounds that inhibit BFT-3 bind to BFT-3 at an exosite, an allosteric site distant from the orthosteric active site. In fact, this idea about acting on cofactor-free alternative conformations under physiological conditions had already been explored previously for other protein targets. GSK484 is an inhibitor of PADI4 (or PAD4, protein-arginine deiminase type-4, another protein associated with cancer) that acts on the calcium-free conformation of PADI4 [93].

Interestingly, in a recent publication focusing on conditionally disordered proteins, such as those dependent on metal cofactors, it is stated that future research should aim to identify and target transient or condition specific structural states for therapeutic interventions—an emerging but challenging frontier in drug discovery [94]. In another recent publication, the potential of targeting folding intermediates and conformational transitions to unlock therapeutic opportunities for IDPs is foreseen [95]. An equivalent approach has been proposed at the cellular level, involving the selection of particular cellular states as targets for drug discovery [96,97].

And this is what we propose as a hypothesis for HDAC8 in this manuscript: HDAC8 is a conditionally disordered zinc-dependent protein that at low zinc concentrations adopts a partially unfolded and inactive conformation that may be targeted for drug discovery. Thus, small molecules binding and stabilizing the Zn^{2+}-free, partially unfolded, inactive state of HDAC8 may act as allosteric inhibitors, providing a new mechanism of action leading to isoform-specific, selective inhibitors of this zinc-dependent enzyme. This underscores the relevance of particular conformational protein states for drug discovery.

A video file (*PCA_global.mp4*) displaying the summary of the global PCA analysis of the simulated Zn^{2+}-bound and Zn^{2+}-free systems is also provided by the authors as Supporting Information. Supplementary data to this article can be found online at https://doi.org/10.1016/j.ijbiomac.2025.149851.

CRediT authorship contribution statement

Paula M. Garcia-Franco: Writing – review & editing, Writing – original draft, Visualization, Validation, Investigation, Formal analysis, Data curation. **F. Javier Falcó-Martí:** Writing – review & editing, Visualization, Validation, Software, Investigation, Formal analysis, Data curation. **Hajar Jeblaoui:** Writing – review & editing, Visualization, Validation, Investigation, Formal analysis, Data curation. **Marta Asencio del Rio:** Writing – review & editing, Visualization, Validation, Investigation, Formal analysis, Data curation. **David Ortega-Alarcon:** Writing – review & editing, Visualization, Validation, Investigation, Formal analysis, Data curation. **Sonia Vega:** Writing – review & editing, Visualization, Validation, Formal analysis. **Juan J. Galano-Frutos:** Writing – review & editing, Writing – original draft, Visualization, Validation, Supervision, Software, Resources, Methodology, Investigation, Formal analysis, Data curation, Conceptualization. **Olga Abian:** Writing – review & editing, Writing – original draft, Visualization, Validation, Supervision, Software, Resources, Project administration, Methodology, Investigation, Funding acquisition, Data curation, Conceptualization. **Adrian Velazquez-Campoy:** Writing – review & editing, Writing – original draft, Visualization, Validation, Supervision, Software, Resources, Project administration, Methodology,

Investigation, Funding acquisition, Formal analysis, Conceptualization.

Funding statement

This work was supported by the Ministerio de Ciencia e Innovación MCIN/AEI/10.13039/501100011033/, Ministerio de Ciencia, Innovación y Universidades MICIU/AEI/10.13039/501100011033/, and "ERDF A way of Making Europe" [PID2021-127296OB-I00 and PID2024-160408OB-I00 to A.V.C.]; Fondo de Investigaciones Sanitarias from Instituto de Salud Carlos III and European Union (ERDF/ESF, "Investing in your future") [PI21/00394 to O.A.]; Gobierno de Aragón [PROY_B08_24 to O.A.]; Ministerio de Economía y Competitividad [BES-2017-080739 to D.O.A.]; Ministerio de Ciencia, Innovación y Universidades [Juan de la Cierva Contract JDC2023-052992-I to D.O.A.]; Ministerio de Ciencia e Innovación with funds from the European Union NextGenerationEU (PRTR-C17.I1) and Gobierno de Aragón within the framework of the Biotechnology Plan Applied to Health (LA3); Gobierno de Aragón [Predoctoral Research Contract 2023–2027 to H.J.]; Instituto de Salud Carlos III [i-PFIS Contract IFI23/00020 to M.A.R.); Gobierno de Aragón [Protein Targets and Bioactive Compounds Group E45_23R to A. V.C., and Digestive Pathology Group B25_23R to O.A.]; and Centro de Investigación Biomédica en Red en Enfermedades Hepáticas y Digestivas (CIBERehd).

Declaration of competing interest

The authors declare the following financial interests/personal relationships which may be considered as potential competing interests: Adrian Velazquez-Campoy reports financial support was provided by Spain Ministry of Science and Innovation. Olga Abian reports financial support was provided by Carlos III Health Institute. Adrian Velazquez-Campoy reports financial support was provided by Government of Aragón. Olga Abian reports financial support was provided by Government of Aragón. If there are other authors, they declare that they have no known competing financial interests or personal relationships that could have appeared to influence the work reported in this paper.

Data availability

Data will be made available on request.

References

[1] A.T. Annunziato, J.C. Hansen, Role of histone acetylation in the assembly and modulation of chromatin structures, Gene Expr. 9 (1–2) (2000) 37–61.
[2] L. Verdone, M. Caserta, E. Di Mauro, Role of histone acetylation in the control of gene expression, Biochem. Cell Biol. 83 (3) (2005) 344–353.
[3] A. Eberharter, P.B. Becker, Histone acetylation: a switch between repressive and permissive chromatin, EMBO Rep. 3 (3) (2002) 224–229.
[4] Y.-J.C. Chen, E. Koutelou, S.Y.R. Dent, Now open: evolving insights to the roles of lysine acetylation in chromatin organization and function, Mol. Cell 82 (4) (2022) 716–727.
[5] M. Wakamori, K. Okabe, K. Ura, T. Funatsu, M. Takinoue, T. Umehara, Quantification of the effect of site-specific histone acetylation on chromatin transcription rate, Nucleic Acids Res. 48 (22) (2020) 12648–12659.
[6] S. Kumar, D. Attrish, A. Srivastava, J. Banerjee, M. Tripathi, P.S. Chandra, A. B. Dixit, Non-histone substrates of histone deacetylases as potential therapeutic targets in epilepsy, Expert Opin. Ther. Targets 25 (1) (2021) 75–85.
[7] M.A. Glozak, N. Sengupta, X. Zhang, E. Seto, Acetylation and deacetylation of non-histone proteins, Gene 363 (2005) 15–23.
[8] P. Wang, Z. Wang, J. Liu, Role of HDACs in normal and malignant hematopoiesis, Mol. Cancer 19 (1) (2020) 5.
[9] M. Haberland, R.L. Montgomery, E.N. Olson, The many roles of histone deacetylases in development and physiology: implications for disease and therapy, Nat. Rev. Genet. 10 (1) (2009) 32–42.
[10] P. Gallinari, S. Di Marco, P. Jones, M. Pallaoro, C. Steinkühler, HDACs, histone deacetylation and gene transcription: from molecular biology to cancer therapeutics, Cell Res. 17 (3) (2007) 195–211.
[11] J.Y. Kim, H. Cho, J. Yoo, G.W. Kim, Y.H. Jeon, S.W. Lee, S.H. Kwon, Pathological role of HDAC8: cancer and beyond, Cells 11 (19) (2022) 3161.
[12] J.J. Buggy, M.L. Sideris, P. Mak, D.D. Lorimer, B. McIntosh, J.M. Clark, Cloning and characterization of a novel human histone deacetylase, HDAC8, Biochem. J. 350 (Pt 1) (2000) 199–205.
[13] E. Hu, Z. Chen, T. Fredrickson, Y. Zhu, R. Kirkpatrick, G.F. Zhang, K. Johanson, C. M. Sung, R. Liu, J. Winkler, Cloning and characterization of a novel human class I histone deacetylase that functions as a transcription repressor, J. Biol. Chem. 275 (20) (2000) 15254–15264.
[14] I. Van den Wyngaert, W. de Vries, A. Kremer, J. Neefs, P. Verhasselt, W.H. Luyten, S.U. Kass, Cloning and characterization of human histone deacetylase 8, FEBS Lett. 478 (1–2) (2000) 77–83.
[15] A. Chakrabarti, I. Oehme, O. Witt, G. Oliveira, W. Sippl, C. Romier, R.J. Pierce, M. Jung, HDAC8: a multifaceted target for therapeutic interventions, Trends Pharmacol. Sci. 36 (7) (2015) 481–492.
[16] J.R. Somoza, R.J. Skene, B.A. Katz, C. Mol, J.D. Ho, A.J. Jennings, C. Luong, A. Arvai, J.J. Buggy, E. Chi, J. Tang, B.C. Sang, E. Verner, R. Wynands, E.M. Leahy, D.R. Dougan, G. Snell, M. Navre, M.W. Knuth, R.V. Swanson, D.E. McRee, L. W. Tari, Structural snapshots of human HDAC8 provide insights into the class I histone deacetylases, Structure 12 (7) (2004) 1325–1334.
[17] D.P. Dowling, S.G. Gattis, C.A. Fierke, D.W. Christianson, Structures of metal-substituted human histone deacetylase 8 provide mechanistic inferences on biological function, Biochemistry 49 (24) (2010) 5048–5056.
[18] A. Chakrabarti, J. Melesina, F.R. Kolbinger, I. Oehme, J. Senger, O. Witt, W. Sippl, M. Jung, Targeting histone deacetylase 8 as a therapeutic approach to cancer and neurodegenerative diseases, Future Med. Chem. 8 (13) (2016) 1609–1634.
[19] J. Naka Wu, C. Du, Z. Lv, C. Ding, J. Cheng, H. Xie, L. Zhou, S. Zheng, The up-regulation of histone deacetylase 8 promotes proliferation and inhibits apoptosis in hepatocellular carcinoma, Dig. Dis. Sci. 58 (12) (2013) 3545–3553.
[20] S. Song, Y. Wang, P. Xu, R. Yang, Z. Ma, S. Liang, G. Zhang, The inhibition of histone deacetylase 8 suppresses proliferation and inhibits apoptosis in gastric adenocarcinoma, Int. J. Oncol. 47 (5) (2015) 1819–1828.
[21] M.Y. Ahn, J.H. Yoon, Histone deacetylase 8 as a novel therapeutic target in oral squamous cell carcinoma, Oncol. Rep. 37 (1) (2017) 540–546.
[22] X. Tang, G. Li, F. Su, Y. Cai, L. Shi, Y. Meng, Z. Liu, J. Sun, M. Wang, M. Qian, Z. Wang, X. Xu, Y.X. Cheng, W.G. Zhu, B. Liu, HDAC8 cooperates with SMAD3/4 complex to suppress SIRT7 and promote cell survival and migration, Nucleic Acids Res. 48 (6) (2020) 2912–2923.
[23] D.A. Moreno, C.A. Scrideli, M.A.A. Cortez, R. De Paula Queiroz, E.T. Valera, V. Da Silva Silveira, J.A. Yunes, S.R. Brandalise, L.G. Tone, Differential expression of HDAC3, HDAC7 and HDAC9 is associated with prognosis and survival in childhood acute lymphoblastic leukaemia, Br. J. Haematol. 150 (6) (2010) 665–673.
[24] J.Y. Kim, H. Cho, J. Yoo, G.W. Kim, Y.H. Jeon, S.W. Lee, S.H. Kwon, HDAC8 deacetylates HIF-1α and enhances its protein stability to promote tumor growth and migration in melanoma, Cancers 15 (4) (2003) 1123.
[25] A. Vannini, C. Volpari, G. Filocamo, E.C. Casavola, M. Brunetti, D. Renzoni, P. Chakravarty, C. Paolini, R. De Francesco, P. Gallinari, C. Steinkühler, S. Di Marco, Crystal structure of a eukaryotic zinc-dependent histone deacetylase, human HDAC8, complexed with a hydroxamic acid inhibitor, Proc. Natl. Acad. Sci. U. S. A. 101 (42) (2004) 15064–15069.
[26] C. Micelli, G. Rastelli, Histone deacetylases: structural determinants of inhibitor selectivity, Drug Discov. Today 20 (6) (2015) 718–735.
[27] F. Yang, N. Zhao, D. Ge, Y. Chen, Next-generation of selective histone deacetylase inhibitors, RSC Adv. 9 (34) (2019) 19571–19583.
[28] G. Shanmugam, S. Rakshit, K. Sarkar, HDAC inhibitors: targets for tumor therapy, immune modulation and lung diseases, Transl. Oncol. 16 (2022) 101312.
[29] Q. Zhao, H. Liu, J. Peng, H. Niu, J. Liu, H. Xue, W. Liu, X. Liu, H. Hao, X. Zhang, J. Wu, HDAC8 as a target in drug discovery: function, structure and design, Eur. J. Med. Chem. 280 (2024) 116972.
[30] R.R. Shah, Safety and tolerability of histone deacetylase (HDAC) inhibitors in oncology, Drug Saf. 42 (2) (2019) 235–245.
[31] C. Andreini, L. Banci, I. Bertini, A. Rosato, Zinc through the three domains of life, J. Proteome Res. 5 (11) (2006) 3173–3178.
[32] C. Andreini, L. Banci, I. Bertini, A. Rosato, Counting the zinc-proteins encoded in the human genome, J. Proteome Res. 5 (1) (2006) 196–201.
[33] X. Arias-Moreno, O. Abian, S. Vega, J. Sancho, A. Velazquez-Campoy, Protein-cation interactions: structural and thermodynamic aspects, Curr. Protein Pept. Sci. 12 (4) (2011) 325–338.
[34] S. Vega, J.L. Neira, C. Marcuello, A. Lostao, O. Abian, A. Velazquez-Campoy, NS3 protease from hepatitis C virus: biophysical studies on an intrinsically disordered protein domain, Int. J. Mol. Sci. 14 (7) (2013) 13282–13306.
[35] O. Abian, J.L. Neira, A. Velazquez-Campoy, Thermodynamics of zinc binding to hepatitis C virus NS3 protease: a folding by binding event, Proteins 77 (3) (2009) 624–636.
[36] A. Jimenez-Alesanco, U. Eckhard, M. Asencio Del Río, S. Vega, T. Guevara, A. Velazquez-Campoy, F.X. Gomis-Rüth, O. Abian, Repositioning small molecule drugs as allosteric inhibitors of the BFT-3 toxin from enterotoxigenic *Bacteroides fragilis*, Protein Sci. 31 (10) (2022) e4427.
[37] H. Fraga, E. Papaleo, S. Vega, A. Velazquez-Campoy, S. Ventura, Zinc induced folding is essential for TIM15 activity as an mtHsp70 chaperone, Biochim. Biophys. Acta, Gen. Subj. 1830 (1) (2013) 2139–2149.
[38] M.A. Aras, E. Aizenman, Redox regulation of intracellular zinc: molecular signaling in the life and death of neurons, Antioxid. Redox Signal. 15 (8) (2011) 2249–2263.
[39] W. Maret, Analyzing free zinc(II) ion concentrations in cell biology with fluorescent chelating molecules, Metallomics 7 (2) (2015) 202–211.
[40] M. Marek, T.B. Shaik, S. Duclaud, R.J. Pierce, C. Romier, Large-scale overproduction and purification of recombinant histone deacetylase 8 (HDAC8) from the human-pathogenic flatworm *Schistosoma mansoni*, in: S. Sarkar (Ed.), Histone Deacetylases, Methods in Molecular Biology, 1436, Humana Press, New York, 2016.

[41] C.N. Pace, B.A. Shirley, J.A. Thomson, in: T.E. Creighton (Ed.), Measuring the Conformational Stability of a Protein, in 'Protein Structure. A Practical Approach', IRL Press, Oxford, 1989, pp. 311–330.
[42] T. Wu, J. Yu, Z. Gale-Day, A. Woo, A. Suresh, M. Hornsby, J.E. Gestwicki, Three essential resources to improve differential scanning fluorimetry (DSF) experiments, 2020, https://doi.org/10.1101/2020.03.22.002543.
[43] O. Abian, S. Vega, J.L. Neira, A. Velazquez-Campoy, Conformational stability of hepatitis C virus NS3 protease, Biophys. J. 99 (11) (2010) 3811–3820.
[44] S. Vega, O. Abian, A. Velazquez-Campoy, Handling complexity in biological interactions, J. Therm. Anal. Calorim. 138 (2019) 3229–3248.
[45] S. Vega, O. Abian, A. Velazquez-Campoy, A unified framework based on the binding polynomial for characterizing biological systems by isothermal titration calorimetry, Methods 76 (2015) 99–115.
[46] E.C. Meng, T.D. Goddard, E.F. Pettersen, G.S. Couch, Z.J. Pearson, J.H. Morris, T. E. Ferrin, U.C.S.F. ChimeraX, Tools for structure building and analysis, Protein Sci. 32 (11) (2023) e4792.
[47] C.R. Søndergaard, M.H.M. Olsson, M. Rostkowski, J.H. Jensen, Improved treatment of ligands and coupling effects in empirical calculation and rationalization of pKa values, J. Chem. Theory Comput. 7 (7) (2011) 2284–2295.
[48] M.H.M. Olsson, C.R. Søndergaard, M. Rostkowski, J.H. Jensen, PROPKA3: consistent treatment of internal and surface residues in empirical pKa predictions, J. Chem. Theory Comput. 7 (2) (2011) 525–537.
[49] S. Unni, Y. Huang, R.M. Hanson, M. Tobias, S. Krishnan, W.W. Li, J.E. Nielsen, N. A. Baker, Web servers and services for electrostatics calculations with APBS and PDB2PQR, J. Comput. Chem. 32 (7) (2011) 1488–1491.
[50] T.J. Dolinsky, J.E. Nielsen, J.A. McCammon, N.A. Baker, PDB2PQR: an automated pipeline for the setup of Poisson-Boltzmann electrostatics calculations, Nucleic Acids Res. 32 (Web Server issue) (2004) W665–W667.
[51] P. Li, K.M. Merz, MCPB.Py: a Python based metal center parameter builder, J. Chem. Inf. Model. 56 (4) (2016) 599–604.
[52] D.A. Case, H.M. Aktulga, K. Belfon, D.S. Cerutti, G.A. Cisneros, V.W.D. Cruzeiro, N. Forouzesh, T.J. Giese, A.W. Götz, H. Gohlke, S. Izadi, K. Kasavajhala, M. C. Kaymak, E. King, T. Kurtzman, T.S. Lee, P. Li, J. Liu, T. Luchko, R. Luo, M. Manathunga, M.R. Machado, H.M. Nguyen, K.A. O'Hearn, A.V. Onufriev, F. Pan, S. Pantano, R. Qi, A. Rahnamoun, A. Risheh, S. Schott-Verdugo, A. Shajan, J. Swails, J. Wang, H. Wei, X. Wu, Y. Wu, S. Zhang, S. Zhao, Q. Zhu, T. E. Cheatham 3rd, D.R. Roe, A. Roitberg, C. Simmerling, D.M. York, M.C. Nagan, K. M. Merz Jr., AmberTools, J. Chem. Inf. Model. 63 (20) (2023) 6183–6191.
[53] M.J. Frisch, G.W. Trucks, H.B. Schlegel, G.E. Scuseria, M.A. Robb, J.R. Cheeseman, G. Scalmani, V. Barone, G.A. Petersson, H. Nakatsuji, X. Li, M. Caricato, A. V. Marenich, J. Bloino, B.G. Janesko, R. Gomperts, B. Mennucci, H.P. Hratchian, J. V. Ortiz, A.F. Izmaylov, J.L. Sonnenberg, D. Williams-Young, F. Ding, F. Lipparini, F. Egidi, J. Goings, B. Peng, A. Petrone, T. Henderson, D. Ranasinghe, V. G. Zakrzewski, J. Gao, N. Rega, G. Zheng, W. Liang, M. Hada, M. Ehara, K. Toyota, R. Fukuda, J. Hasegawa, M. Ishida, T. Nakajima, Y. Honda, O. Kitao, H. Nakai, T. Vreven, K. Throssell, J.A. Montgomery Jr., J.E. Peralta, F. Ogliaro, M. J. Bearpark, J.J. Heyd, E.N. Brothers, K.N. Kudin, V.N. Staroverov, T.A. Keith, R. Kobayashi, J. Normand, K. Raghavachari, A.P. Rendell, J.C. Burant, S.S. Iyengar, J. Tomasi, M. Cossi, J.M. Millam, M. Klene, C. Adamo, R. Cammi, J.W. Ochterski, R.L. Martin, K. Morokuma, O. Farkas, J.B. Foresman, D.J. Fox, Gaussian 16, Gaussian Inc, Wallingford CT, 2016 https://gaussian.com/gaussian16/.
[54] C. Tian, K. Kasavajhala, K.A.A. Belfon, L. Raguette, H. Huang, A.N. Migues, J. Bickel, Y. Wang, J. Pincay, Q. Wu, C. Simmerling, Ff19SB: amino-acid-specific protein backbone parameters trained against quantum mechanics energy surfaces in solution, J. Chem. Theory Comput. 16 (1) (2020) 528–552.
[55] H.J.C. Berendsen, D. van der Spoel, R. van Drunen, GROMACS: a message-passing parallel molecular dynamics implementation, Comput. Phys. Commun. 91 (1995) 43–56.
[56] E. Lindahl, B. Hess, D. van der Spoel, GROMACS 3.0: a package for molecular simulation and trajectory analysis, J. Mol. Model. 7 (2001) 306–317.
[57] D. van der Spoel, E. Lindahl, B. Hess, G. Groenhof, A.E. Mark, H.J.C. Berendsen, GROMACS: fast, flexible and free, J. Comput. Chem. 26 (2005) 1701–1718.
[58] W.L. Jorgensen, J. Chandrasekhar, J.D. Madura, W.R.W. Impey, M.L. Klein, Comparison of simple potential functions for simulating liquid water, J. Chem. Phys. 79 (2) (1983) 926–935.
[59] P. Li, L.F. Song, K.M. Merz Jr., Systematic parameterization of monovalent ions employing the nonbonded model, J. Chem. Theory Comput. 11 (4) (2015) 1645–1657.
[60] G. Bussi, D. Donadio, M. Parrinello, Canonical sampling through velocity rescaling, J. Chem. Phys. 126 (1) (2007) 014101.
[61] H.J.C. Berendsen, J.P.M. Postma, W.F. van Gunsteren, A. DiNola, J.R. Haak, Molecular-dynamics with coupling to an external bath, J. Chem. Phys. 81 (1984) 3684–3690.
[62] M. Parrinello, A. Rahman, Polymorphic transitions in single crystals: a new molecular dynamics method, J. Appl. Phys. 52 (12) (1981) 7182–7190.
[63] T. Darden, D. York, L. Pedersen, Particle mesh Ewald: an N·log(N) method for Ewald sums in large systems, J. Chem. Phys. 98 (12) (1993) 10089–10092.
[64] B. Hess, H. Bekker, H.J.C. Berendsen, J.G.E.M. Fraaije, LINCS: a linear constraint solver for molecular simulations, J. Comput. Chem. 18 (12) (1997) 1463–1472.
[65] H. Garcia-Cebollada, J.J. Galano-Frutos, J. Sancho, reMoDA: automated calculation of unfolding detection metrics for relaxation Molecular Dynamics, 2024. Available from: https://github.com/elhectro2/reMoDA.
[66] R.T. McGibbon, K.A. Beauchamp, M.P. Harrigan, C. Klein, J.M. Swails, C. X. Hernandez, C.R. Schwantes, L.P. Wang, T.J. Lane, V.S. Pande, MDTraj: a modern open library for the analysis of molecular dynamics trajectories, Biophys. J. 109 (8) (2015) 1528–1532.
[67] W. Kabsch, C. Sander, Dictionary of protein secondary structure: pattern recognition of hydrogen-bonded and geometrical features, Biopolymers 22 (12) (1983) 2577–2637.
[68] Y. Zhang, J. Skolnick, Scoring function for automated assessment of protein structure template quality, Proteins Struct. Funct. Bioinf. 57 (4) (2004) 702–710.
[69] J. Estrada, P. Bernado, M. Blackledge, J. Sancho, ProtSA: a web application for calculating sequence specific protein solvent accessibilities in the unfolded ensemble, BMC Bioinf. 10 (2009) 104.
[70] P. Bernado, M. Blackledge, J. Sancho, Sequence-specific solvent accessibilities of protein residues in unfolded protein ensembles, Biophys. J. 91 (2006) 4536–4543.
[71] E. Jurrus, D. Engel, K. Star, K. Monson, J. Brandi, L.E. Felberg, D.H. Brookes, L. Wilson, J. Chen, K. Liles, M. Chun, P. Li, D.W. Gohara, T. Dolinsky, R. Konecny, D.R. Koes, J.E. Nielsen, T. Head-Gordon, W. Geng, R. Krasny, G.W. Wei, M.J. Holst, J.A. McCammon, N.A. Baker, Improvements to the APBS biomolecular solvation software suite, Protein Sci. 27 (1) (2018) 112–128.
[72] A. Vannini, C. Volpari, P. Gallinari, P. Jones, M. Mattu, A. Carfí, R. De Francesco, C. Steinkühler, S. Di Marco, Substrate binding to histone deacetylases as shown by the crystal structure of the HDAC8-substrate complex, EMBO Rep. 8 (9) (2007) 879–884.
[73] G. Bohm, R. Muhr, R. Jaenicke, Quantitative analysis of protein far UV circular dichroism spectra by neural networks, Protein Eng. 5 (3) (1992) 191–195.
[74] R.W. Woody, Circular dichroism, Methods Enzymol. 246 (1995) 34–71.
[75] S.M. Kelly, N.C. Price, The use of circular dichroism in the investigation of protein structure and function, Curr. Protein Pept. Sci. 1 (4) (2000) 349–384.
[76] J.T. Vivian, P.R. Callis, Mechanisms of tryptophan fluorescence shifts in proteins, Biophys. J. 80 (5) (2001) 2093–2109.
[77] A. Velazquez-Campoy, J. Sancho, O. Abian, S. Vega, Biophysical screening for identifying pharmacological chaperones and inhibitors against conformational and infectious diseases, Curr. Drug Targets 17 (13) (2016) 1492–1505.
[78] M. Bastos, O. Abian, C.M. Johnson, F. Ferreira-da-Silva, S. Vega, A. Jimenez-Alesanco, D. Ortega-Alarcon, A. Velazquez-Campoy, Isothermal titration calorimetry, Nat. Rev. Methods Primers 3 (2023) 17.
[79] M.B. Kunze, D.W. Wright, N.D. Werbeck, J. Kirkpatrick, P.V. Coveney, D. F. Hansen, Loop interactions and dynamics tune the enzymatic activity of the human histone deacetylase 8, J. Am. Chem. Soc. 135 (47) (2013) 17862–17868.
[80] H. Keller, P. Gottwald, N. Wendling, The role of zinc in carbonic anhydrase, Biochem. Biophys. Res. Commun. 3 (1) (1960) 24–27.
[81] A.I.S. Moretti, V.E. Baksheeva, A.Y. Roman, T.C. De Bessa, F. Devred, H. Kovacic, P.O. Tsvetkov, Exploring the influence of zinc ions on the conformational stability and activity of protein disulfide isomerase, Int. J. Mol. Sci. 25 (4) (2024) 2095.
[82] P. Cimmperman, L. Baranauskiene, S. Jachimoviciūte, J. Jachno, J. Torresan, V. Michailoviene, J. Matuliene, J. Sereikaite, V. Bumelis, D. Matulis, A quantitative model of thermal stabilization and destabilization of proteins by ligands, Biophys. J. 95 (7) (2008) 3222–3231.
[83] J. Rösgen, H.J. Hinz, Phase diagrams: a graphical representation of linkage relations, J. Mol. Biol. 328 (1) (2003) 255–271.
[84] X. Arias-Moreno, A. Velazquez-Campoy, J.C. Rodríguez, M. Pocovi, J. Sancho, Mechanism of low density lipoprotein (LDL) release in the endosome: implications of the stability and Ca2+ affinity of the fifth binding module of the LDL receptor, J. Biol. Chem. 283 (33) (2008) 22670–22679.
[85] B. Chen, P. Yu, W.N. Chan, F. Xie, Y. Zhang, L. Liang, K.T. Leung, K.W. Lo, J. Yu, G. M.K. Tse, W. Kang, K.F. To, Cellular zinc metabolism and zinc signaling: from biological functions to diseases and therapeutic targets, Signal Transduct. Target. Ther. 9 (1) (2024) 6.
[86] M.W. Thompson, Regulation of zinc-dependent enzymes by metal carrier proteins, Biometals 35 (2) (2022) 187–213.
[87] B. Kim, A.S. Pithadia, C.A. Fierke, Kinetics and thermodynamics of metal-binding to histone deacetylase 8, Protein Sci. 24 (3) (2015) 354–365.
[88] C.A. Castaneda, J.E. Lopez, C.G. Joseph, M.D. Scholle, M. Mrksich, C.A. Fierke, Active site metal identity alters histone deacetylase 8 substrate selectivity: a potential novel regulatory mechanism, Biochemistry 56 (42) (2017) 5663–5670.
[89] X. Liu, A. Jimenez-Alesanco, Z. Li, B. Rizzuti, J.L. Neira, M. Estaras, L. Peng, E. Chuluyan, J. Garona, F. Gottardo, A. Velazquez-Campoy, Y. Xia, O. Abian, P. Santofimia-Castaño, J. Iovanna, Development of an efficient NUPR1 inhibitor with anticancer activity, Sci. Rep. 14 (1) (2024) 29515.
[90] P. Santofimia-Castaño, Y. Xia, W. Lan, Z. Zhou, C. Huang, L. Peng, P. Soubeyran, A. Velazquez-Campoy, O. Abian, B. Rizzuti, J.L. Neira, J. Iovanna, Ligand-based design identifies a potent NUPR1 inhibitor exerting anticancer activity via necroptosis, J. Clin. Invest. 129 (6) (2019) 2500–2513.
[91 J.L. Neira, J. Bintz, M. Arruebo, B. Rizzuti, T. Bonacci, S. Vega, A. Lanas, A. Velazquez-Campoy, J.L. Iovanna, O. Abian, Identification of a drug targeting an intrinsically disordered protein involved in pancreatic adenocarcinoma, Sci. Rep. 7 (2017) 39732.
[92] O. Abian, S. Vega, J. Sancho, A. Velazquez-Campoy, Allosteric inhibitors of the NS3 protease from the hepatitis C virus, PLoS One 8 (7) (2013) e69773.
[93] H.D. Lewis, J. Liddle, J.E. Coote, S.J. Atkinson, M.D. Barker, B.D. Bax, K.L. Bicker, R.P. Bingham, M. Campbell, Y.H. Chen, C.W. Chung, P.D. Craggs, R.P. Davis, D. Eberhard, G. Joberty, K.E. Lind, K. Locke, C. Maller, K. Martinod, C. Patten, O. Polyakova, C.E. Rise, M. Rüdiger, R.J. Sheppard, D.J. Slade, P. Thomas, J. Thorpe, G. Yao, G. Drewes, D.D. Wagner, P.R. Thompson, R.K. Prinjha, D. M. Wilson, Inhibition of PAD4 activity is sufficient to disrupt mouse and human NET formation, Nat. Chem. Biol. 11 (3) (2015) 189–191.
[94] B. Devi, N. Nag, V.N. Uversky, T. Tripathi, Conditional disorder in proteins: functional transitions between order and disorder, Chem. Commun. 61 (85) (2025) 16512–16528.

[95] L.F. Kjaer, F.S. Ielasi, T. Winbolt, E. Delaforge, M. Tengo, L. Mamigonian Bessa, L. Mariño Perez, E. Boeri Erba, G. Bouvignies, A. Palencia, M. Ringkjøbing Jensen, Hierarchical folding-upon-binding of an intrinsically disordered protein, Nat. Commun. (2025), https://doi.org/10.1038/s41467-025-66420-5.

[96] T. Cañeque, L. Baron, S. Müller, A. Carmona, L. Colombeau, A. Versini, S. Solier, C. Gaillet, F. Sindikubwabo, J.L. Sampaio, M. Sabatier, E. Mishima, A. Picard-Bernes, L. Syx, N. Servant, B. Lombard, D. Loew, J. Zheng, B. Proneth, L. K. Thoidingjam, L. Grimaud, C.S. Fraser, K.J. Szylo, E. Der Kazarian, C. Bonnet, E. Charafe-Jauffret, C. Ginestier, P. Santofimia-Castaño, M. Estaras, N. Dusetti, J. L. Iovanna, A. Sa Cunha, G. Pittau, P. Hammel, D. Tzanis, S. Bonvalot, S. Watson, V. Gandon, A. Upadhyay, D.A. Pratt, F. Porto Freitas, J.P. Friedmann Angeli, B. R. Stockwell, M. Conrad, J.M. Ubellacker, R. Rodriguez, Activation of lysosomal iron triggers ferroptosis in cancer, Nature 642 (8067) (2025) 492–500.

[97] G.S. França, M. Baron, B.R. King, J.P. Bossowski, A. Bjornberg, M. Pour, A. Rao, A. S. Patel, S. Misirlioglu, D. Barkley, K.H. Tang, I. Dolgalev, D.A. Liberman, G. Avital, F. Kuperwaser, M. Chiodin, D.A. Levine, T. Papagiannakopoulos, A. Marusyk, T. Lionnet, I. Yanai, Cellular adaptation to cancer therapy along a resistance continuum, Nature 631 (8022) (2024) 876–883.